10-30-2015

Novel Ternary Magnesium-Tin Alloys by Microalloying

Sadegh Behdad
Florida International University, sbehd001@fiu.edu

DOI: 10.25148/etd.FIDC000209

FLORIDA INTERNATIONAL UNIVERSITY

Miami, Florida

NOVEL TERNARY MAGNESIUM-TIN ALLOYS BY MICROALLOYING

A dissertation submitted in partial fulfillment of the

requirements for the degree of

DOCTOR OF PHILOSOPHY

in

MATERIALS SCIENCE AND ENGINEERING

by

Sadegh Behdad

2015

To: Interim Dean Ranu Jung
College of Engineering and Computing

This dissertation, written by Sadegh Behdad, and entitled Novel Ternary Magnesium-Tin Alloys by Microalloying, having been approved in respect to style and intellectual content, is referred to you for judgment. We have read this dissertation and recommend that it be approved.

Bilal El-Zhab

Hassan Mahfuz

W. Kinzy Jones

Arvind Agarwal, Co-Major Professor

Benjamin Boesl, Co-Major Professor

Date of Defense: October 30, 2015

The dissertation of Sadegh Behdad is approved.

Interim Dean Ranu Jung
College of Engineering

Dean Lakshmi N. Reddi
University Graduate School

Florida International University, 2015

DEDICATION

I dedicate this dissertation to my parents and to all my teachers who have inspired me.

ACKNOWLEDGMENTS

This dissertation is the result of collective effort of many people. It would not have been possible for me to complete my research without their endless support and contributions.

I sincerely thank my advisor, Dr. Benjamin Boesl, for supporting me and letting me take the lead in choosing the topic of my PhD research. He showed me how to start off an academic career and how to collaborate with other researchers. He always motivated me in days of frustration and encouraged me to push myself to grow more.

I would also like to thank Dr. Arvind Agarwal, for his kind and critical guidance and for being a great mentor. He gave me the most needed scientific and professional advise. I will never forget how he changed my life. He is a man of many talents. I learned a lot about time management and multi-tasking working with him. His round-the-clock encouragement inspired me to work harder every day.

My heartfelt gratitude goes to Dr. Kinzy Jones for being such an amazing guru and visionary. He was my advisor for the first three and a half years of my PhD. He selflessly supported my transition to a new research group and yet contributed to my research and publications till the very last day. He has devoted his life to train his students to be team players. He showed me how to lead by example and not by command. His dedication to his colleagues' and students' career is matched by no other. It is impossible for me to thank him enough for all he has done for me in the past six years. He set an example how an advisor should be and I cannot think one could be better than that. I wish I could become like him one day.

I am thankful to Dr. Cesar Levy for all his dedication to support me and all the other students in the Mechanical and Materials Engineering department. Words can not express my gratitude towards him.

I would like to thank Dr. Michele V. Manuel and members of Materials Design & Prototyping Laboratory at University of Florida for helping me cast my alloys. I sincerely thank Dr. Hunter B. Henderson and Dr. Zachary L. Bryan for their help in casting Magnesium alloys and their helpful discussions. I also thank Ryan J. Hooper for his very helpful conversation on grain refinement in Magnesium alloys.

I sincerely thank Dr. Yongho Sohn and members of Advanced Materials Processing and Analysis Center (AMPAC) and Laboratory of Materials and Coatings for Extreme Conditions at University of Central Florida. I acknowledge Dr. Le Zhou and Dr. Catherine Kammerer for their help in conducting and analysis of HRTEM and diffusion experiments. Catherine was not only a great scholar but also a role model and a close friend for me. I would also like to thank Clara Hofmeister, Abhishek Mehta, and Esin Geller to devote hours to help me make my diffusion couples. I made friends for life in the summer of 2014 at University of Central Florida.

I sincerely thank Dr. Bilal El-Zahab and Dr. Hassan Mahfuz for serving on my dissertation committee and for their timely advice and support throughout my PhD research. Dr. El-Zahab was very helpful during the initial stages of my research and provided me immense help with the research facilities in his lab.

I would like to thank Pranjal Nautiyal for his helpful discussions on Nano-indentation creep. Our relationship goes beyond colleagues. He is like my younger brother. He dedicated hours to discuss and double-check my calculations. I cannot thank him enough for all his help.

My sincere thanks to Cheng Zhang and Chris Rudolph for helping me conduct my XRD experiments and for lending me hands whenever I needed help from them during my research.

I also acknowledge all staff and technicians of Advanced Materials Research Institute (AMERI) for their help during my PhD. My heartfelt thanks to Dr. Emirov for spending hours with me to conduct TEM experiments. He was always willing to help me.

I am thankful to University Graduate School at Florida International University for supporting me through Dissertation Evidence Acquisition (DEA) and Dissertation Year Fellowship (DYF) awards.

My special thanks to my colleagues and friends, Dr. Ali Karbasi, Ali Hadjikhani, Hari Adluru and Roozbeh Nikkhah. They were always there for me, whenever I need any help, be it technical or personal. They were like my brothers. Ali Karbasi helped from the very first day. I learnt a lot from him and even today when I need any technical help, I do not hesitate to contact him. Ali Hadjikhani has been an extraordinary friend; it is rare to find friends like them. I always shared my frustrations with Hari and Roozbeh and they always inspired me to follow my dreams.

Lastly, this section will be incomplete without mentioning about another influential person in my life – Dr. Siamak Moradian. I learnt a lot from him in different aspects of life. He was a great advisor. He taught me things I will remember for life.

ABSTRACT OF THE DISSERTATION

NOVEL TERNARY MAGNESIUM-TIN ALLOYS BY MICROALLOYING

by

Sadegh Behdad

Florida International University, 2015

Miami, Florida

Professor Arvind Agarwal, Co-Major Professor

Benjamin Boesl, Co-Major Professor

The objective of this research was to explore the possibility of developing novel Magnesium-Tin alloys with improved mechanical properties by micro-alloying. Magnesium is the lightest of all structural metals. It can be machined faster and with almost half the power required for aluminum. There is a limitless supply of magnesium in sea water and it can also be recycled at 5% of initial energy requirements. These properties make magnesium an ideal green alternative to replace metals and polymers in automotive, aerospace, biomedical and defense sectors. The potential weight reduction in the US automotive market alone, leads to 100 billion gallons of gas saved and 6.5 billion gallons of CO2 emissions reduced per year.

In defense and aerospace markets, China is the leading foreign supplier of rare earth metals necessary for fabrication of current high-performance Mg alloys, making core defense technologies vulnerable to the interruption of Chinese imports. In the past, China has used its control over mining, application and import of rare earth metals as a strategic leverage. These new Magnesium-Tin ternary alloys offer an alternative that can be made from domestic resources improving national security and minimizing foreign dependence on rare earth metals import.

Our results establish that microalloying can tackle issues arising from sluggish precipitate formation kinetics and precipitate size distribution in binary Magnesium-Tin alloys. These new alloys also offer an order of magnitude reduction in heat treatment time (from approximately 1000 hours to less than 100 hours), which makes the benefits of their application two-fold by decreasing manufacturing energy costs and production time. This can also open the route for development of new age-hardenable wrought Magnesium alloys.

TABLE OF CONTENTS

LIST OF TABLES

TABLE PAGE

LIST OF FIGURES

FIGURE PAGE

1. Motivation

The objective of this research is to develop a new Magnesium-Tin alloy for automotive applications. Magnesium is the lightest of all structural metals. With a density of 1738 kg/m^3, it has almost one quarter the weight of steel and two-thirds the weight of aluminum. It is the eighth most abundant element in the earth's crust. There is a virtually limitless supply of magnesium in sea water. Magnesium has very good strength to weight ratio. Its melting point is 923 K and its specific heat is 1020 J/kg.K. Therefore, it is easily cast by conventional methods to desired shape with uniform properties. It can be machined faster and with less power than aluminum [1], as well as recycled at 5% of initial energy requirements for its extraction [2]. These properties have led to an increased attention to development of Mg alloys for applications where potential weight savings can be beneficial such as automotive [3,4], aerospace [5-7], and biomedical sectors [8-11].

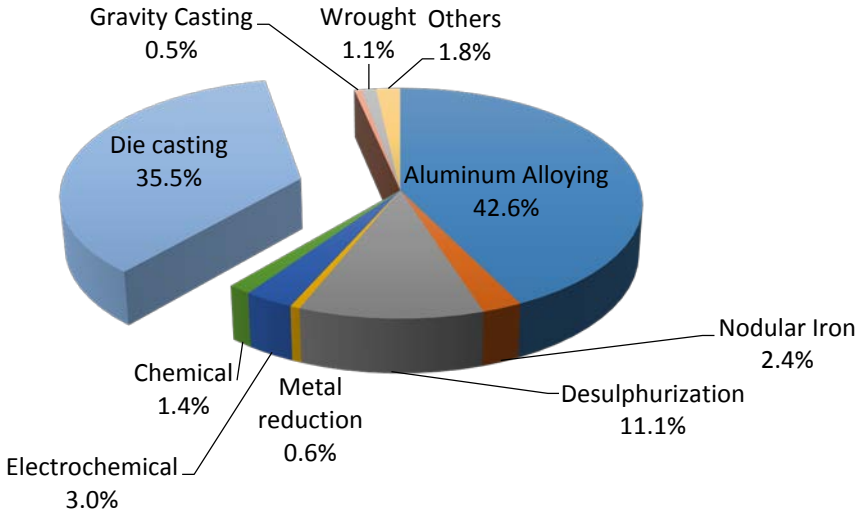

Figure 1.1. Global magnesium market segments in 1999 [12]

The total global production of primary magnesium has almost doubled in 2001-2010 period, reaching 809,000 metric tons in 2010 according to International Magnesium Association. Market share of various industries in magnesium consumption is shown in Figure 1.1. Die-casting has the second biggest share among market segments [12]. The main industrial application of magnesium die cast alloys is the automotive industry, where their light weight contributes to fuel saving and lower emissions.

Utilization of such alloys in engine parts would lead to better fuel economy and in turn, reduce carbon dioxide emissions and environmental damages from vehicles. As an example, currently an average car has 3.5 kilograms of magnesium whereas about 18 kilograms of magnesium is used in different drivetrain components in Volkswagen Group vehicles. It is predicted that usage of magnesium parts in gearbox housing, mountings, oil pump, oil pump housing, and crankcase can increase the magnesium usage by another 14-20 kg in the next 5-10 years [12]. Assuming that all these parts are now made of aluminum, this replacement will lead to a 20-25% weight decrease (~3.5-5 kg). For every 100 kg weight reduction, the fuel consumption will reduce 0.3 L for a small car and 0.4 L for a light truck per 100 km [13]. According to world energy council, the average annual travel distance of a vehicle in US is 17,500 km. Every 100 kg decrease in weight reduces CO_2 emissions by 9 gr/km. Therefore, such weight reduction will result in 2788 L (736 US gal) less CO_2 emissions and 183.75 L (48.54 US gal) less gas for each car per year. There are more than 135 million passenger cars in US; that is almost 100 billion gallons of gas and 6.5 billion gallons of CO_2 emissions per year just for passenger cars in US alone.

Currently, the benchmark magnesium casting alloys in the automotive industry are AZ91, AM50, and AM60 [12,14]. Aluminum is the major alloying element in all three alloys. Aluminum is usually added to magnesium in order to improve castability by extending the freezing range, increasing fluidity and ductility and room temperature tensile properties [15,16]. These alloys are restricted to applications in which the service temperature does not exceed 120°C. This limitation is directly due to a change in material properties as a function of elevated temperature. This degradation in property is particularly evident in the elevated temperature creep behavior of current alloys as shown in Figure 1.2. Further substantial increase of magnesium alloys usage requires development of new alloys that have adequate strength and creep resistance in 150-200 °C temperature range.

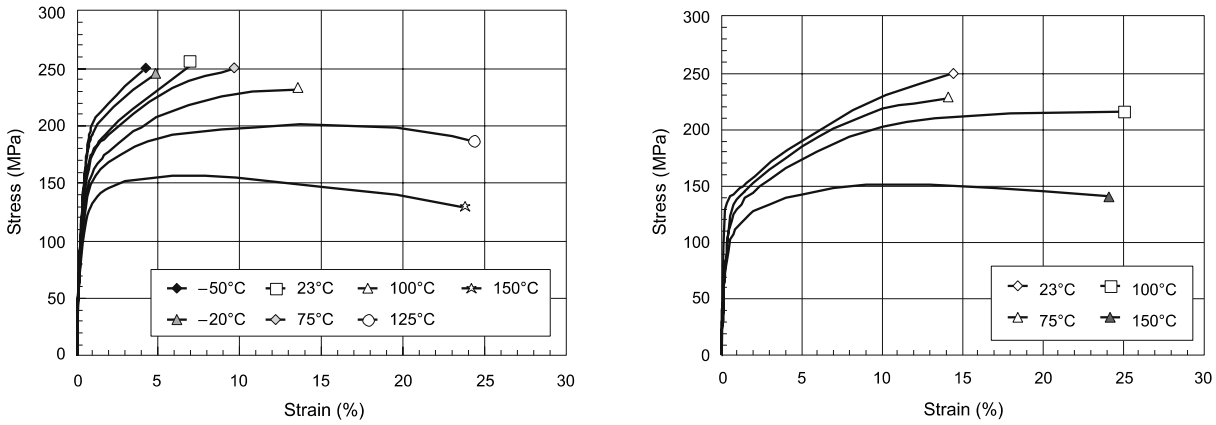

Figure 1.2. Tensile Stress-Strain curves of a) AZ91 (Left) and b) AM60 (Right) [12]

The main present alternative for elevated temperature applications is AE42, which can be used at service temperatures up to 170 °C [17]. Above this temperature, decomposition of the interdendritic lamellar phase $Al_{11}RE_3$ leads to an abrupt degradation of creep resistance [16,17]. Rare earths have also been added to Mg-Zn alloys to improve their mechanical properties at elevated temperatures [18-21]. These efforts have led to

development of MEZ alloy which has better creep resistance than AE42 in 150-175 °C temperature range [22]. At temperatures up to 300 °C, Yttrium containing Mg alloys exhibit very good creep resistance and a corrosion performance on par with high purity aluminum alloys [12,23]. Despite their superior properties, application of commercially available Mg-Y-RE alloys, i.e. WE43 and WE54, has been limited to aerospace, F1 racing cars, and motor sports where added benefits can compensate for the economic disadvantage [22,24]. Relatively high cost of rare earths is the main drawback that limits applications of all the above-mentioned alloy families. Mg-Sn alloys can potentially fill the gap in the market for an affordable Mg alloy that exhibits comparable performance.

Maximum solid solubility of Tin in Magnesium is almost 3.45 at.% (14.85 wt.%) with the eutectic temperature 561 °C, and decreases to 0.1 at% at 200 °C, which makes it ideal for precipitate formation. It forms Mg_2Sn precipitate with a melting point of 770 °C, even higher than the melting point of the intermetallics formed in binary Mg-Gd, Mg-Y, and Mg-RE counterparts as shown in Table 1.1 [25]. Therefore, there is potential for the development of Mg-Sn alloys for elevated temperature applications.

Mg_2Sn precipitate is face-centered cubic, point group $m\bar{3}m$, and a=0.676 nm [26,27]. However, the precipitation process by artificial aging below 300 °C does not develop any metastable phases and the precipitates in Mg-Sn binary alloy are very coarse compared to other precipitate forming Mg alloys [28]. In order to develop an alloy with proper strength, precipitation size distribution in Mg-Sn must be modified. It has been proposed that microalloying (i.e. adding less than 1 at. % of an alloying element) might be useful in controlling the precipitation size and accelerating aging kinetics [29-34]. The goal of this

dissertation is to explore the possibility of developing novel Mg-Sn alloys by micro-alloying additions of Titanium (Ti) or Hafnium (Hf).

Table 1.1. Melting point of precipitation phases in binary Mg alloy systems [25]

System	Phase	Melting Point (°C)
Mg-Ag	Mg_3Ag	492
Mg-Al	$Mg_{17}Al_{12}$	402
Mg-Ca	Mg_2Ca	714
Mg-Ce	$Mg_{12}Ce$	611
Mg-Er	$Mg_{24}Er_5$	620
Mg-Gd	Mg_6Gd	640
Mg-In	Mg_3In	484
Mg-Nd	$Mg_{41}Nd_5$	560
Mg-Pb	Mg_2Pb	538
Mg-Pr	$Mg_{12}Pr$	585
Mg-Sn	Mg_2Sn	770
Mg-Th	$Mg_{23}Th_6$	772
Mg-Tm	$Mg_{24}Tm_6$	645
Mg-Y	$Mg_{24}Y_5$	620
Mg-Yb	Mg_2Yb	718
Mg-Zn	MgZn	347

In the automotive industry, the materials cost has a major share in the final price, and a successful commercial alloy should have acceptable elevated temperature properties coupled with affordable cost. This is an area where Mg-Sn alloys can potentially target to have a major impact on the market. Table 1.2 compares the cost of raw materials per unit weight of our proposed alloys to some of the commercially available alloys. It can be seen that raw materials needed for production of these alloys cost almost half of the cheapest commercial alloy in the market.

Table 1.2. Cost of raw materials per unit weight of alloy

Alloy	Mg-Sn-Ti	Mg-Sn-Hf	AE42	WE43	ZRE1
Price ($)	15.36	21.45	32.36	91.94	50.42

Literature review

Deformation Behavior of Magnesium

Magnesium has hexagonal close-packed crystal structure. According to von Mises criterion, a polycrystalline material requires at least 5 independent shear systems to accommodate homogeneous deformation under strain to maintain its initial volume. A list of possible slip systems in hexagonal close-packed metals is shown in Table 1.3.

Table 1.3. Independent slip systems in hcp metals [35]

Slip system	Burgers vector	Slip direction	Slip plane	No. of slip systems	
				Total	Independent
1	a	$< 11\bar{2}0 >$	Basal (0001)	3	2
2	a	$< 11\bar{2}0 >$	Prismatic type I $\{10\bar{1}0\}$	3	2
3	a	$< 11\bar{2}0 >$	Pyramidal type I $\{10\bar{1}1\}$	6	4
4	a+c	$< 11\bar{2}3 >$	Pyramidal type II $\{11\bar{2}2\}$	6	5
5	c	$< 0001 >$	Prismatic type I $\{10\bar{1}0\}$	3	2
6	c	$< 0001 >$	Prismatic type II $\{11\bar{2}0\}$	3	2

However, extensive studies on deformation behavior of Magnesium show that basal slip is the only deformation mode that is active over a wide range of temperature [35-38]. When the loading is exerted parallel to basal plane, non-basal slip will be more favorable. Under such conditions, prismatic <a> glide will be the preferred deformation mode at

room temperature [39,40]. A total of 4 independent slip systems are provided by these two systems, which can be active simultaneously.

Since the shape change in crystal structure due to pyramidal <a> slip can be produced by a combination of the above mentioned deformation mode, it is not counted as an independent deformation mode. Other pyramidal slip systems are only activated at temperatures above 200 °C [41]. Therefore, Magnesium does not have a sufficient number of shear systems to satisfy von Mises criterion at room temperature. This limited capability of Magnesium and its alloys for plastic deformation at room temperature has major implications for Magnesium alloy development as discussed below.

Effect of Deformation Behavior on Mg Alloy Development

Commercially available wrought alloys of Magnesium only comprise of Mg-Al-Zn (AZ), Mg-Mn (M), and Mg-Zn-Zr (ZK) alloys. As seen in Figure 1.1, wrought alloys have slightly above 1% share in the annual Magnesium consumption. Lack of steady development of Mg wrought alloys is a result of limited workability of Magnesium at room temperature. When traditional deformation processes like extrusion and rolling are used at high temperatures necessary for deformation of Magnesium alloys, dynamic recrystallization leads to significant grain growth [42]. Hall-Petch coefficient of Mg is ~700 $kPa.m^{-1/2}$, making it more susceptible to lose its mechanical properties with grain growth.

In contrary, Magnesium has excellent casting properties because it is easily pourable and shows good mould-filling properties [12]. Automotive industry has been the major leading force of Mg casting alloy development with a specific interest in die cast alloys [4,14].

Magnesium Alloying

Selection of Alloying Element in Magnesium Alloys

Selection of alloying elements mainly depends on the alloying method. When using non-conventional methods such as sintering, mechanical alloying, co-spray, etc. the selection pool is large. However, most alloying companies still rely on conventional molten metal processing, where extensive liquid solubility is required. If the difference in electronegativity of the alloying element and Magnesium is large, it leads to formation of stable compounds that usually decrease liquid solubility. In some cases such as Si, Mn, and Zr, even though the liquid solubility is fairly sufficient, the temperature required for substantial dissolution is too high [12,43].

Another major factor in alloy design is solid solubility of alloying elements as it plays an important role in processing and mechanical properties of the alloy [43]. Solid solubility is affected by atomic size of the elements. As a general rule, the difference between the atomic size of alloying element and Mg must be less than 15% in order to achieve good solid solubility. Figure 1.3 shows the range of atomic sizes for different elements in comparison with Magnesium.

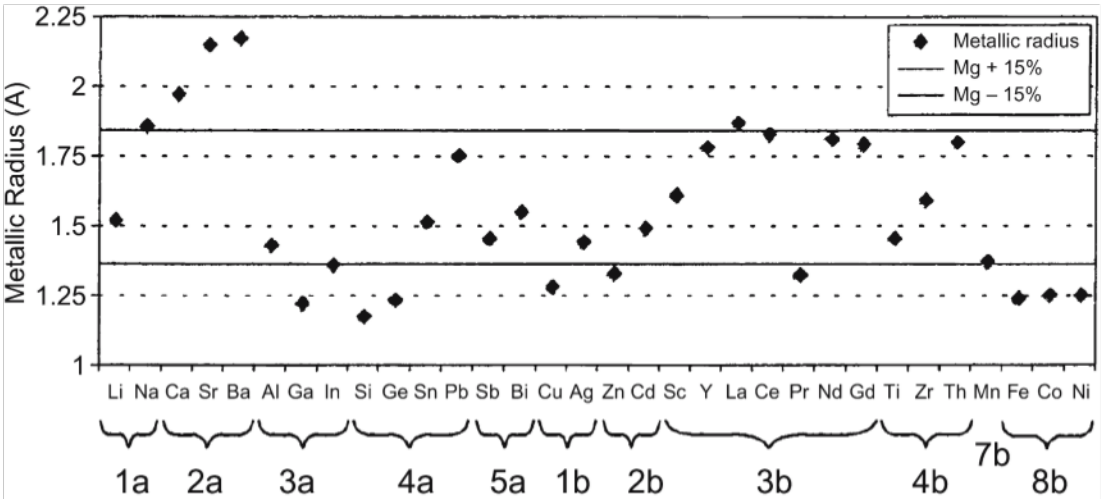

Figure 1.3. Atomic size of different metals [12]

These two factors limit the usage of many elements as major alloying element for Magnesium. It can be seen from Figure 1.3 that solely based on metallic radius values, there are almost 25 elements that can be alloyed with Magnesium. But after considering the liquid solubility and temperature required for processing of the resultant alloy (Figure 1.4), the number of alloying elements that are actually used in industrial practice reduces to only about ten elements: Al, Zn, Mn, Li, Ag, Gd, Y, RE, Ca, and Zr.

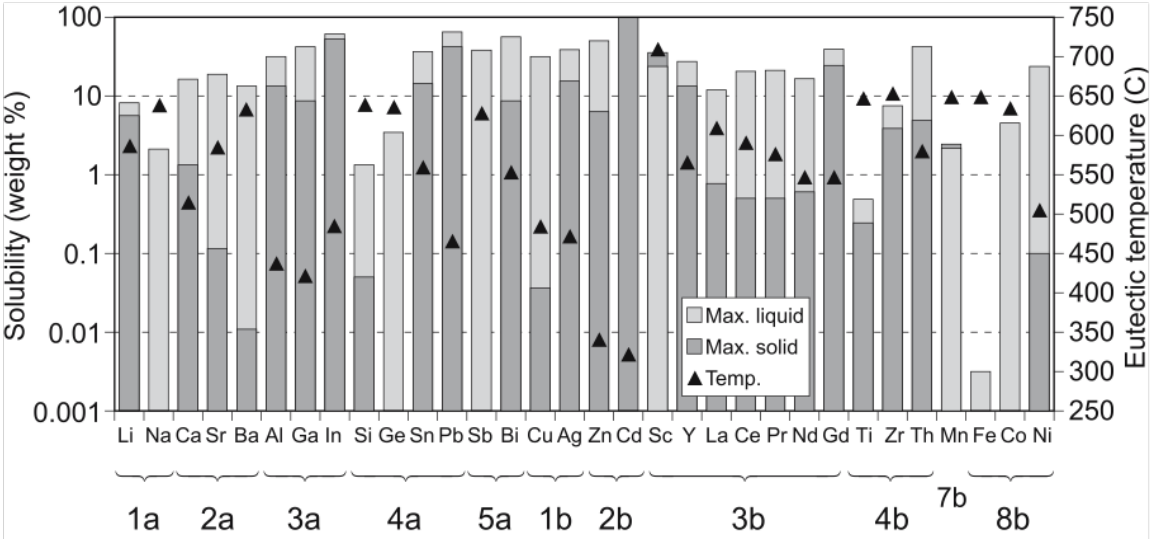

Figure 1.4. Max. solid and liq. solubility and eutectic temperatures of binary Mg systems [12]

Therefore, there is a need for methods that allow incorporation of other elements in Mg alloys in order to tailor their properties and extend their applications. One of these methods is microalloying, i.e. addition of small amounts (~<0.1-0.2 at.%) of selected elements. It has been known for some time that certain additions in similar systems will yield to a disproportionate gain in properties and considerable cost savings [44,45]. In the following section, theoretical aspects of how microalloying can be beneficial in Magnesium alloy development are discussed.

Theories on Microalloying in Magnesium Alloys

Thermokinetic Criterion

Mendis et al. proposed qualitative thermo-kinetic criteria to select microalloying elements in order to refine precipitation distribution in a hypothetical Mg-X system and tested their criteria in microalloying Mg-Sn as a model magnesium alloy [30]. They suggest that if a third alloying element (Y) is added to the Mg-X (here, X: Sn) binary system, which meets the following criteria, it is very likely that Y can facilitate the nucleation stage of precipitate formation:

1) Y has a thermodynamic tendency to form heterogeneities such as clusters or co-clusters upon cooling after the solution treatment. This is represented by a miscibility gap in Mg-Y binary phase diagram.

2) Y and X do not have any “repulsive tendency”. Y atoms won’t act as effective nucleation centers if they repel X atoms.

3) Y can form finer precipitates/clusters in a faster time scale than X. Otherwise, addition of Y would not increase nucleation rate. Although, very little is known about clustering kinetics in magnesium alloys, diffusivity of the microalloying element is expected to affect it and therefore, it was used to prioritize the choices for microalloying.

Following the same method, by using binary Mg-X and Sn-X phase diagrams the choice of the following elements has been proposed in the previous research: Hf, Mo, Na, Nb, Rb, Ti, V. To fulfill the second criteria, the chosen element should not be among the set of elements that segregate from major alloying element. In case of Sn, element Y can’t be selected from Al, Be, Cr, Ga, Ge, Rb, Zn. Based on the diffusivities of the remaining elements, the prioritized choices will be Na, Hf, Ti, Nb, Mo, and V.

Based on the proposed criteria, Na was chosen as microalloying element and an Mg-1.3Sn-0.15Na (at.%) alloy was synthesized by induction melting. It was observed that such addition increased peak hardness increment and decreased the time to reach peak hardness from ~1000 hours to a very practical 58 hours. The change in the number of precipitates and their average dimensions is shown in Table 1.4. As can be seen, the number of the precipitates increases by two orders of magnitude and there is a size reduction in length, width and thickness of the lath shaped precipitates upon Na addition.

Table 1.4. Quantitative measurements of precipitates in Mg-Sn alloys at maximum hardness at 200 °C [30]

Alloy composition (*at.* %)	N_v x 10^{18} (m^{-3})	$\bar{l}$ *(nm)*	$\overline{w}$ *(nm)*	$\bar{t}$ *(nm)*	$\frac{\bar{l}}{\overline{w}}$	$\frac{\bar{l}}{\bar{t}}$
Mg-1.3 Sn	0.6	1500 ±400	500 ±80	54 ±11	3	28
Mg-1.3 Sn-0.15 Na	56.4	230 ± 50	90 ±22	25 ±8.5	2.55	9.2

Following research reported similar improvements in Mg-Sn-Na-Zn [31] and Mg-Sn-Al-Zn-Na systems [46]. 3-D atomic probe mapping of alloys revealed strong enrichment of Al at precipitate/matrix interface and enrichment of Na and Zn in the precipitates. Co-clustering of Na and Sn atoms was also observed in 3DAP maps (Fig.1.5).

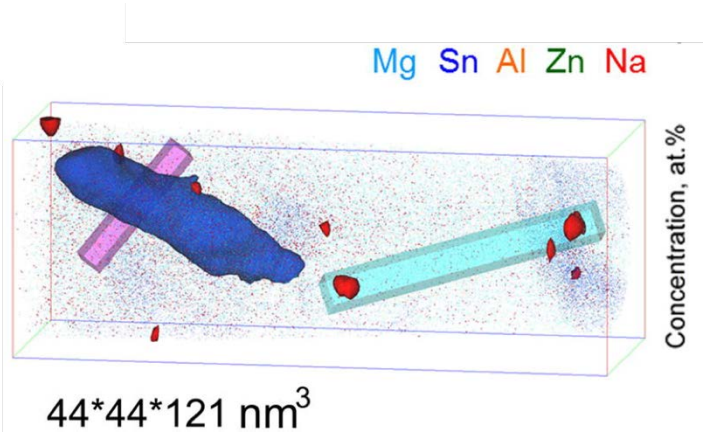

Figure 1.5. 3-D atomic probe mapping of peak-aged Mg–10Sn–3Al–1Zn–0.1Na at 160 °C [46]

Shear Strain Energy Accommodation Criterion

Modeling results show that high aspect ratio plate-shaped precipitates, such as those observed in Yttrium-RE Magnesium alloys, are the most effective barriers to dislocation glide on basal plane in Magnesium [47]. Since these precipitates are stronger than Mg matrix, their formation is associated with a transformation strain with the invariant plane parallel to the shear plane $(1\bar{1}00)$. This leads to formation of areas of contraction and expansion in the matrix around them as shown in Figure 1.6 [6,48,49]. Similar mechanism is suggested for formation of γ′ plates Mg-Y-Zn and Mg-Gd-Zn alloys [28].

A possible route to minimize this shear strain energy is an extrinsic supply of larger solute atoms to expansion regions and corresponding concentrations of vacancies to contraction regions. Gadolinium (180 pm), Yttrium (181 pm), and Neodymium (185 pm), have larger atomic radii than Magnesium (160 pm) and negative binding energies with vacancies [50]. Therefore, their local segregation around precipitates in the extended areas coupled with migration of associated vacancies to the compressed areas can release or totally relieve the shear strain of a precipitate during nucleation (or growth). If such mechanism is at work, then it is reasonable that any new precipitates evolving from such solute rich clusters form at the end facets of the β_1 precipitates rather than on their wide side. Experimental HRTEM and HAADF-STEM evidence in Yttrium-RE Magnesium alloys (WE54) confirm that β′ precipitates form at end facets of the β_1 precipitates in deed (Fig. 1.6). Similar observations are well documented in Al-Cu-Sn alloys, where Sn atoms are always found at the end facets of θ′ plates and formation of θ′ precipitates associated with a large shear strain energy [28]. Atomic radii of Al, Cu, and Sn are 125, 135, and 145 pm respectively. Therefore, the best choice of microalloying element for increasing nucleation of plate-shaped precipitates would be elements with large atomic

radius and high binding energy with vacancies. However, further experimental work is required to prove formation of proposed segregates around precipitate edges. First-principle calculations to find solute-vacancy binding energy for different solutes in Magnesium would also help in better selection of micro-alloying elements according to this theory.

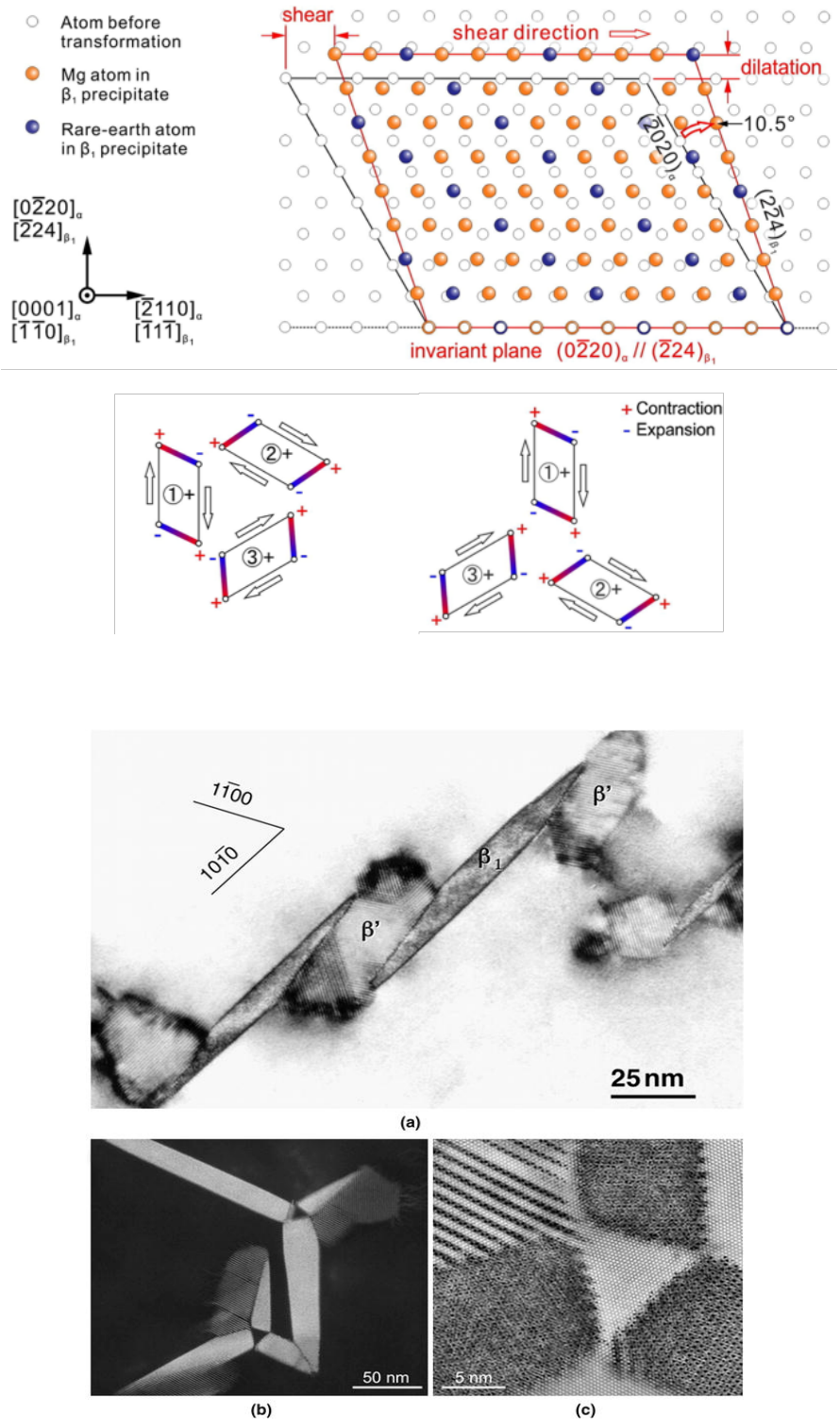

Figure 1.6. Shear accommodation around precipitates in WE54 Mg alloy
Top: Shear strain around β_1 precipitate in WE54 Mg alloy [48]
Bottom: HRTEM and HAADF images of formation of β′ particles on end-facets of β_1 plates precipitates in WE54 Mg alloy [6,49]

Paired Atoms Criterion

It is reported that in Mg-1Gd (at.%) alloy, addition of just 0.4 at.% Zn leads to a significant increase in the as quenched hardness [51]. Solid solution strengthening by such a small amount of Zn addition can't account for the observed change in hardness [52]. 3DAP data didn't show any solute clusters of Zn or Gd either. Nonetheless, statistical analysis of 3DAP data showed that Zn and Gd co-segregate in the as quenched samples. Substitution of magnesium atom (160 pm) by a larger atom, such as Gd or Y atom, results in a positive misfit (~ 12%); and its exchange with Tin (145 pm) or Zinc (135 pm) leads to a negative misfit of about 9% and 16% respectively. Such substitutions will generate areas of compression and extension strain in the lattice. It is plausible that formation of large atom-small atom segregates will reduce the elastic strain on the lattice. On the other hand, no evidence of clusters of Gd or Zn atoms was found in the 3DAP analysis. Therefore, it was deduced that Gd-Zn dimers have formed in the magnesium solid solution. A schematic showing this mechanism is presented in Figure 1.7.

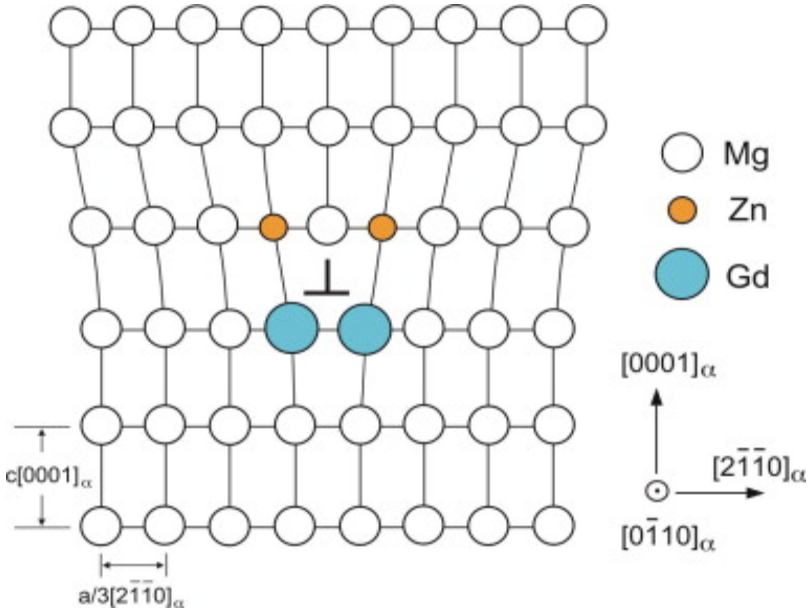

Figure 1.7. Dimers formed by Gd and Zn next to a dislocation in microalloyed Mg-Gd-Zn [53]

Similar dimer formation may justify improvements in creep response of Mg-Y and Mg-Gd alloys by Zn microalloying as well [51,54]. Presence of these dimers around dislocations will lessen lattice strain around both solute atoms and dislocation; this provides a better pinning of sliding dislocations and consequently has a more significant effect on hardness than solid solution hardening alone. If microalloying element's atomic size is selected such that it can form dimers with main alloying element, it can have a major impact on mechanical properties such as hardness and creep resistance.

References:

1. Avedesian MM, Baker H. *ASM specialty handbook: Magnesium and magnesium alloys.* ; 1999:15.

2. Ditze A, Scharf C. *Recycling of magnesium.* Ditze & Scharf; 2008.

3. Easton M, Beer A, Barnett M, et al. Magnesium alloy applications in automotive structures. *JOM*. 2008;60(11):57-62.

4. Luo AA. Recent magnesium alloy development for automotive powertrain applications. . 2003;419:57-66.

5. Aghion E, Bronfin B. Magnesium alloys development towards the 21st century. . 2000;350:19-30.

6. Nie J, Muddle B. Precipitation in magnesium alloy WE54 during isothermal ageing at 250 C. *Scr Mater*. 1999;40(10):1089-1094.

7. Furuya H, Kogiso N, Matunaga S, Senda K. Applications of magnesium alloys for aerospace structure systems. . 2000;350:341-348.

8. Berglund IS, Brar HS, Dolgova N, et al. Synthesis and characterization of Mg- Ca- Sr alloys for biodegradable orthopedic implant applications. *Journal of Biomedical Materials Research Part B: Applied Biomaterials*. 2012;100(6):1524-1534.

9. Kirkland NT, Birbilis N, Walker J, Woodfield T, Dias GJ, Staiger MP. In- vitro dissolution of magnesium–calcium binary alloys: Clarifying the unique role of calcium additions in bioresorbable magnesium implant alloys. *Journal of Biomedical Materials Research Part B: Applied Biomaterials*. 2010;95(1):91-100.

10. Kirkland N, Lespagnol J, Birbilis N, Staiger M. A survey of bio-corrosion rates of magnesium alloys. *Corros Sci*. 2010;52(2):287-291.

11. Brar HS, Wong J, Manuel MV. Investigation of the mechanical and degradation properties of Mg–Sr and Mg–Zn–Sr alloys for use as potential biodegradable implant materials. *Journal of the mechanical behavior of biomedical materials*. 2012;7:87-95.

12. Friedrich HE, Mordike BL. *Magnesium technology.* Springer; 2006.

13. Cheah L, Evans C, Bandivadekar A, Heywood J. *Factor of two: Halving the fuel consumption of new US automobiles by 2035.* Springer; 2009.

14. Luo AA. Recent magnesium alloy development for elevated temperature applications. *International Materials Reviews*. 2004;49(1):13-30.

15. Moreno I, Nandy T, Jones J, Allison J, Pollock T. Microstructural characterization of a die-cast magnesium-rare earth alloy. *Scr Mater*. 2001;45(12):1423-1429.

16. Moreno I, Nandy T, Jones J, Allison J, Pollock T. Microstructural stability and creep of rare-earth containing magnesium alloys. *Scr Mater*. 2003;48(8):1029-1034.

17. Powell BR, Rezhets V, Balogh MP, Waldo RA. Microstructure and creep behavior in AE42 magnesium die-casting alloy. *JOM*. 2002;54(8):34-38.

18. He S, Peng L, Zeng X, Ding W, Zhu Y. Comparison of the microstructure and mechanical properties of a ZK60 alloy with and without 1.3 wt.% gadolinium addition. *Materials Science and Engineering: A*. 2006;433(1):175-181.

19. Zhou H, Zhang Z, Liu C, Wang Q. Effect of nd and Y on the microstructure and mechanical properties of ZK60 alloy. *Materials Science and Engineering: A*. 2007;445:1-6.

20. Zhang J, Ma Q, Pan F. Effects of trace er addition on the microstructure and mechanical properties of Mg–Zn–Zr alloy. *Mater Des*. 2010;31(9):4043-4049.

21. Chen Q, Shu D, Zhao Z, Zhao Z, Wang Y, Yuan B. Microstructure development and tensile mechanical properties of Mg–Zn–RE–Zr magnesium alloy. *Mater Des*. 2012;40:488-496.

22. Aghion E, Bronfin B, Von Buch F, Schumann S, Friedrich H. Newly developed magnesium alloys for powertrain applications. *JOM*. 2003;55(11):30-33.

23. Wang J, Hsiung L, Nieh T, Mabuchi M. Creep of a heat treated Mg–4Y–3RE alloy. *Materials Science and Engineering: A*. 2001;315(1):81-88.

24. Agnew SR. Wrought magnesium: A 21st century outlook. *JOM*. 2004;56(5):20-21.

25. Hort N, Huang Y, Kainer KU. Intermetallics in magnesium alloys. *Advanced Engineering Materials*. 2006;8(4):235-240.

26. Nie J. Precipitation and hardening in magnesium alloys. *Metallurgical and Materials Transactions A*. 2012;43(11):3891-3939.

27. Gibson M, Fang X, Bettles C, Hutchinson C. The effect of precipitate state on the creep resistance of Mg–Sn alloys. *Scr Mater*. 2010;63(8):899-902.

28. Nie J. Precipitation and hardening in magnesium alloys. *Metallurgical and Materials Transactions A*. 2012;43(11):3891-3939.

29. Sasaki T, Oh-Ishi K, Ohkubo T, Hono K. Enhanced age hardening response by the addition of zn in Mg–Sn alloys. *Scr Mater*. 2006;55(3):251-254.

30. Mendis C, Bettles C, Gibson M, Gorsse S, Hutchinson C. Refinement of precipitate distributions in an age-hardenable Mg–Sn alloy through microalloying. *Philosophical magazine letters*. 2006;86(7):443-456.

31. Mendis C, Bettles C, Gibson M, Hutchinson C. An enhanced age hardening response in Mg–Sn based alloys containing zn. *Materials Science and Engineering: A*. 2006;435:163-171.

32. Mendis C, Oh-Ishi K, Hono K. Enhanced age hardening in a Mg–2.4 at.% zn alloy by trace additions of ag and ca. *Scr Mater*. 2007;57(6):485-488.

33. Elsayed F, Sasaki T, Mendis C, Ohkubo T, Hono K. Compositional optimization of Mg–Sn–Al alloys for higher age hardening response. *Materials Science and Engineering: A*. 2013;566:22-29.

34. Huang X, Zhang W, Ma Y, Yin M. Enhancement of hardening and thermal resistance of Mg–Sn-based alloys by addition of cu and al. *Philosophical Magazine Letters*. 2014;94(8):460-469.

35. Partridge P. The crystallography and deformation modes of hexagonal close-packed metals. *Metallurgical reviews*. 1967;12(1):169-194.

36. Burke E, Hibbard W. The plastic deformation of magnesium single crystals. *T. Metall. Soc. AIME*. 1952;194:295.

37. Hauser FE, Landon PR, Dorn JE. *Deformation and fracture mechanisms of polycrystalline magnesium at low temperatures.* Minerals Research Laboratory, Institute of Engineering Research, University of California, Berkeley; 1954.

38. Graff S. *Micromechanical modeling of the deformation of HCP metals*. 2008.

39. Reed-Hill RE, Robertson WD. Deformation of magnesium single crystals by nonbasal slip. *Journal of Metals-Transactions AIME*. 1957;220:496-502.

40. Yoshinaga H, Horiuchi R. Deformation mechanisms in magnesium single crystals compressed in the direction parallel to hexagonal axis. *Transactions of the Japan Institute of Metals*. 1963;4(1):1-8.

41. Reed-Hill R, Robertson W. Pyramidal slip in magnesium. *Trans.Met.Soc.AIME*. 1958;212.

42. Hono K, Mendis C, Sasaki T, Oh-Ishi K. Towards the development of heat-treatable high-strength wrought mg alloys. *Scr Mater*. 2010;63(7):710-715.

43. Raynor GV. *The physical metallurgy of magnesium and its alloys.* Vol 5. Pergamon; 1959.

44. De Garmo EP, Black JT, Kohser RA. *DeGarmo's materials and processes in manufacturing.* John Wiley & Sons; 2011.

45. Somekawa H, Osawa Y, Singh A, Washio K, Kato A, Mukai T. Effect of micro-alloying elements on deformation behavior in Mg–Y binary alloys. *Materials Transactions*. 2014;55(1):182-187.

46. Elsayed F, Sasaki T, Mendis C, Ohkubo T, Hono K. Significant enhancement of the age-hardening response in Mg–10Sn–3Al–1Zn alloy by na microalloying. *Scr Mater*. 2013;68(10):797-800.

47. Nie J. Effects of precipitate shape and orientation on dispersion strengthening in magnesium alloys. *Scr Mater*. 2003;48(8):1009-1015.

48. Xu Z, Weyland M, Nie J. On the strain accommodation of β 1 precipitates in magnesium alloy WE54. *Acta Materialia*. 2014;75:122-133.

49. Nie J, Muddle B. Characterisation of strengthening precipitate phases in a Mg–Y–Nd alloy. *Acta Materialia*. 2000;48(8):1691-1703.

50. Saal JE, Wolverton C. Solute–vacancy binding of the rare earths in magnesium from first principles. *Acta Materialia*. 2012;60(13):5151-5159.

51. Nie JF, Gao X, Zhu SM. Enhanced age hardening response and creep resistance of Mg–Gd alloys containing zn. *Scr Mater*. 2005;53(9):1049-1053.

52. Kammerer CC, Behdad S, Zhou L, et al. Diffusion kinetics, mechanical properties, and crystallographic characterization of intermetallic compounds in the Mg–Zn binary system. *Intermetallics*. 2015;67:145-155.

53. Nie J, Oh-Ishi K, Gao X, Hono K. Solute segregation and precipitation in a creep-resistant Mg–Gd–Zn alloy. *Acta Materialia*. 2008;56(20):6061-6076.

54. Suzuki M, Kimura T, Koike J, Maruyama K. Strengthening effect of zn in heat resistant Mg–Y–Zn solid solution alloys. *Scr Mater*. 2003;48(8):997-1002.

2. Hypothesis

The goal if this research is to investigate the validity of the following hypothesis:

> ***Hypothesis:*** *Microalloying of Mg-Sn alloys with Hf or Ti will result in increased hardening response upon aging and accelerated aging kinetics due to precipitate size refinement.*

Among the elements that can be selected based on Mendis' thermo-kinetic criteria discussed in the previous chapter, microalloying of Mg-Sn model system with Ti and Hf were chosen for this research. Titanium and Hafnium both have hexagonal close-packed structure like Magnesium. Being on the same group of periodic table, Ti and Hf have similar valence electrons and are expected to exhibit similar chemical behavior.

Recently, it has been reported that Ti addition to magnesium alloys can lead to grain refinement [1]. Zirconium is also in this column of periodic table and minute additions of Zr as an effective grain refiner are common in magnesium alloying [2] Therefore, possible additional advantages due to grain refinement after micro-alloying are also examined.

Mg-Sn binary phase diagram and corresponding binary phase diagrams are shown in Figures 2.1 to 2.3 below. It can be seen that binary phase diagrams satisfy Thermokinetic criteria. Mg-Ti and Hf-Mg show negligible solid solubility.

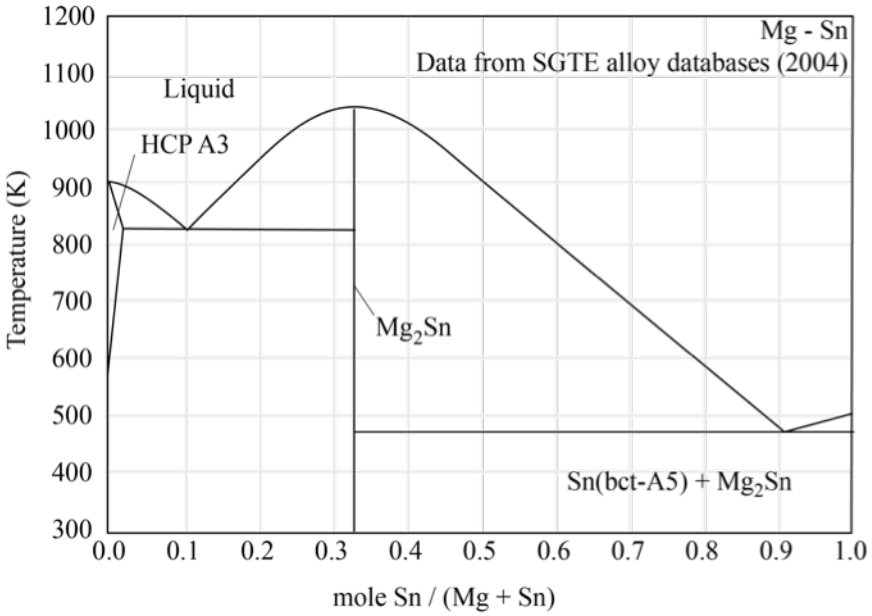

Figure 2.1. Mg-Sn binary phase diagram

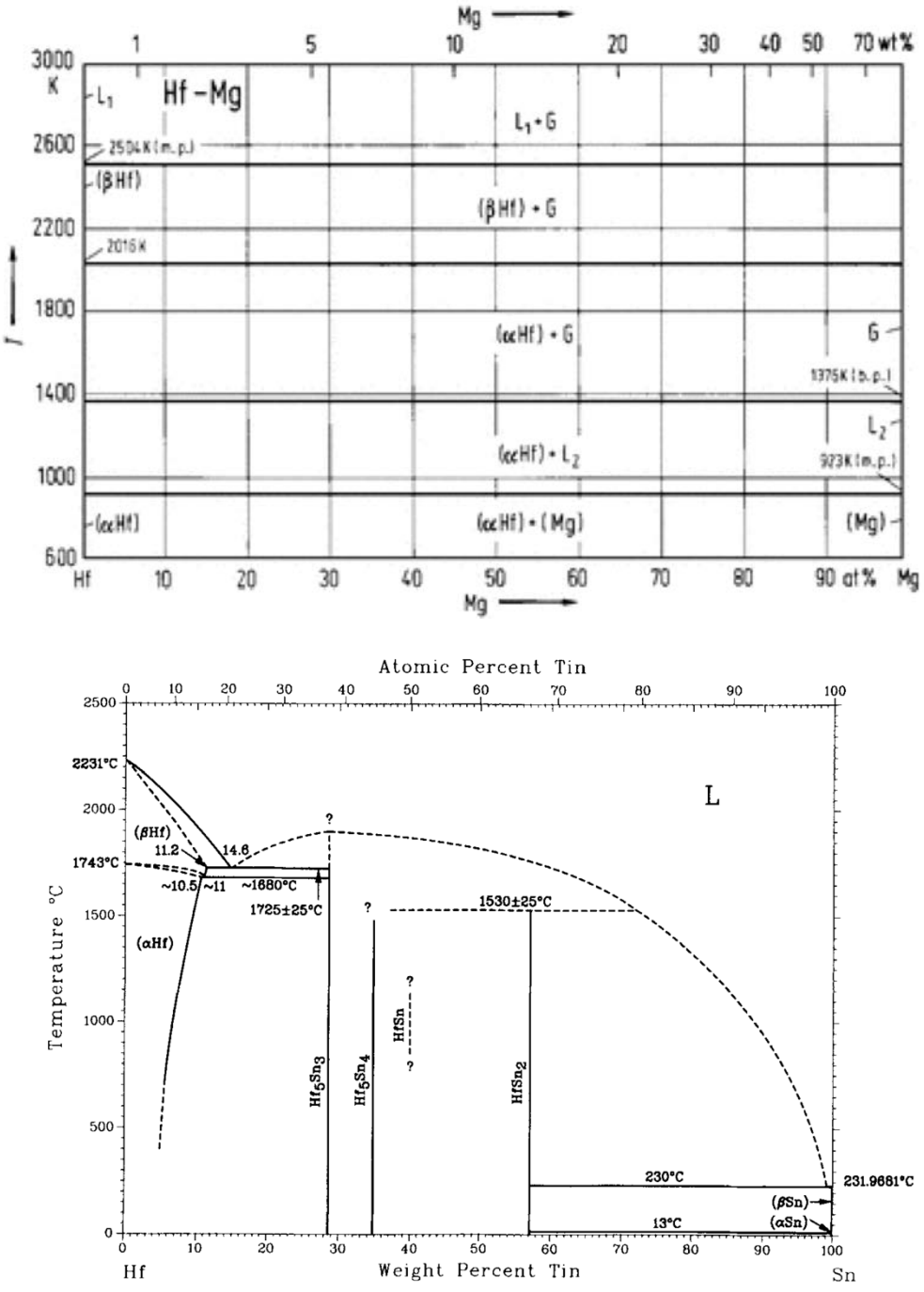

Figure 2.2. Corresponding binary phase diagrams for proposed Mg-Sn-Hf alloy compositions
Top: Hf-Mg [3], Bottom: Hf-Sn [4]

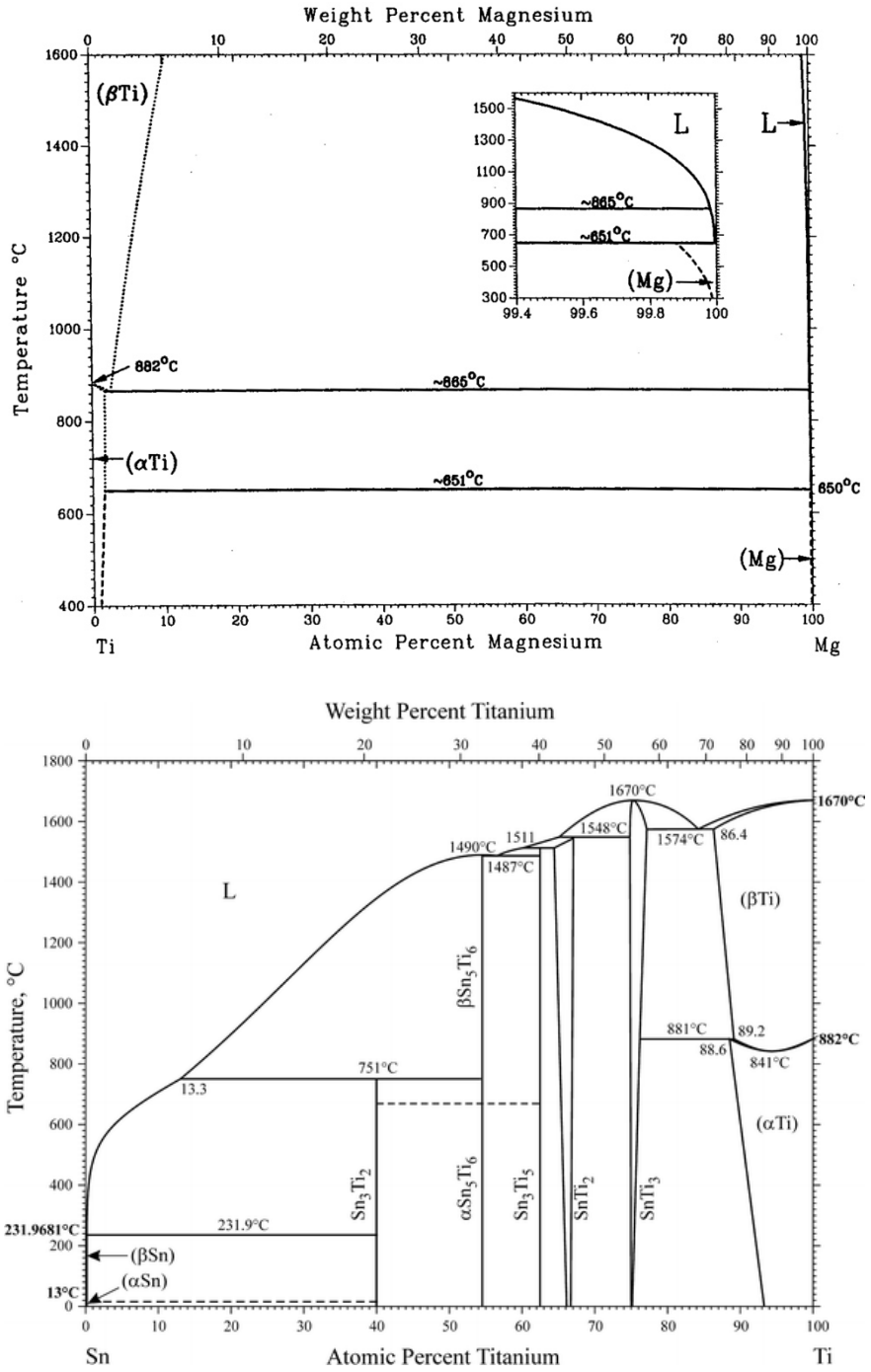

Figure 2.3. Corresponding binary phase diagrams for proposed Mg-Sn-Ti alloy compositions Top: Mg-Ti [5] , Bottom: Sn-Ti [5]

Research outline

The plan to test validity of hypothesis consists of four stages:

1. Alloy synthesis, 2. Artificial Aging, 3. Microstructural characterization, and 4. Nano-mechanical testing.

A flowchart of research stages and experiments is shown in Figure 2.4. These steps are also briefly described below.

Alloy synthesis

Previous studies of mechanical properties and creep resistance of Mg-Sn alloys containing 1-10 wt.% Sn (~0.2-2.3 at.%) reported that 5 wt.% Sn alloy (T5) showed the best tensile strength, while 10 wt.% added Sn (T10) had the highest hardness and better creep resistance than AE42 at 150 °C [6]. Therefore, these two compositions were chosen and the effect of micro-alloying with Ti and Hf additions to them was studied. The composition of all alloys and their designations are presented in Table 3.1 in the Experimental chapter.

Artificial Aging

Age hardening response of the samples was studied by artificial ageing in Silicone oil bath at 200 °C. Vickers hardness measurements was conducted according to ASTM standard E92-82 to evaluate the effects of changes in the microstructure in the early stages of hardening and compare time to peak hardness and hardness increment upon microalloying.

After this step, only T5 and corresponding micro-alloyed samples were selected for micro-structural analysis.

Microstructural Characterization

Grain size distribution of samples was measured by optical microscopy. Energy dispersive spectroscopy (EDS) was performed to verify sample composition. After XRD and SEM were used to characterize present phases and microstructure of the samples, a selected number of samples (T5 and Hf modified samples) were chosen for further TEM analysis.

TEM micrographs were used to measure size, number density, aspect ratio, and morphology of precipitates. Selected samples (T5 and one of Hf modified samples) were picked for additional characterization using HRTEM and HAADF-STEM along with EDXS.

Nano-mechanical Testing

Room temperature mechanical testing was performed on five samples (T5 and corresponding Ti/Hf modified samples) under careful consideration to monitor laboratory conditions and thermal drift to avoid complications in analysis of nano-indentation data. Nano-indentation tests with different holding times in the loading/holding/unloading cycle were used to compare the nano-scale indentation creep response of the samples.

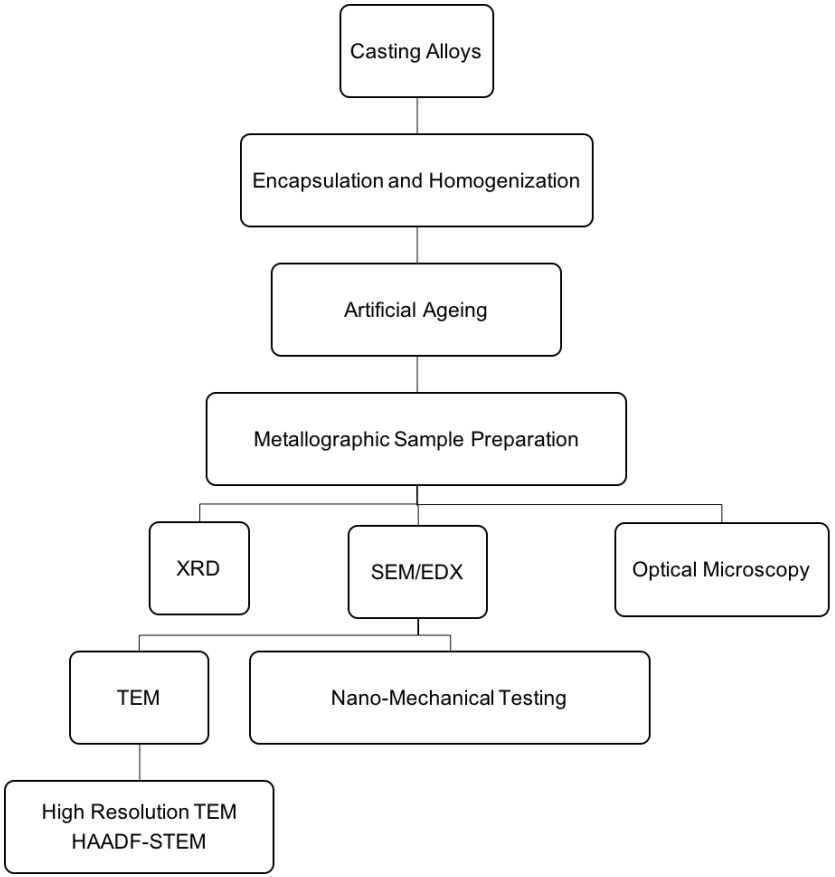

Figure 2.4. Outline of the experiments conducted in this study

References:

1. Buha J. Natural ageing in magnesium alloys and alloying with ti. *J Mater Sci*. 2008;43(4):1220-1227.

2. Friedrich HE, Mordike BL. *Magnesium technology.* Springer; 2006.

3. Predel B, Madelung O. *The landolt-börnstein databas, landolt-börnstein - group IV physical chemistry volume 5f.* SpringerMaterials; 1996.

4. Okamoto H. The hf-sn (hafnium-tin) system. *Journal of phase equilibria*. 1991;12(4):472-474.

5. Murray J. The mg− ti (magnesium-titanium) system. *Bulletin of Alloy Phase Diagrams*. 1986;7(3):245-248.

6. Liu H, Chen Y, Tang Y, Wei S, Niu G. The microstructure, tensile properties, and creep behavior of as-cast mg–(1–10)% sn alloys. *J Alloys Compounds*. 2007;440(1):122-126.

3. Experimental

Materials

High purity metals in form of chips and powders were used for alloy synthesis in this study. The list and specifications of these metals are shown in Table 3.1.

Table 3.1. Specifications of materials used for alloy synthesis

Metal	Specification as provided by vendor	Mesh	Particle size (μm)	Vendor
Mg	Chips, 99.98%	-4+30	595-4760	Sigma-Aldrich
Sn	Powder, 99.85%	-100	< 149	Alfa Aesar
Ti	Powder, spherical, 99.9%	-150	< 100	Alfa Aesar
Hf	Powder, 99.6%	-325	< 44	Alfa Aesar

Alloy Synthesis

A total of ten alloys were synthesized to investigate the hypothesis. Alloy designations and nominal compositions of the samples in both at.% and wt.% is listed in Table 3.2. Hereafter, all samples are described in wt.%. All alloys were measured by Denver Instruments micro-balance, mixed and cast under high purity Argon atmosphere in an mBRAUN glovebox. Oxygen levels were monitored to be less than 10 ppm to prevent oxidation during all the stages.

Alloys were fabricated by melting in a resistance-heating furnace at 750 °C. Molten mixture was stirred with a graphite rod after 30 minutes to ensure proper mixing, and was cast after another 15 minutes in a graphite mold previously sprayed by hexagonal Boron Nitride high temperature release agent. Mould was kept inside the glovebox to cool down to room temperature and then ingots were transferred to open air. A picture of the casting set-up is shown in Figure 3.1.

Encapsulation and Homogenization

Alloys were cut into small pieces and put in quartz tubes. Tubes were vacuumed and backfilled multiple times with Hydrogen and dry high purity Argon to remove any remaining Oxygen and moisture from the tubes. Quartz tubes were then partially pressurized with Ar and sealed for homogenization treatment. For homogenization, alloys were heated to 345 °C at a heating rate of 80 °C/hour and kept at that temperature for 2 hours, then heated to 500 °C at 80 °C/hour rate and kept for 6 hours at 500 °C. Samples were then quenched in cold water. The custom-made vacuum pump used for encapsulation is shown in Figure 3.2.

Table 3.2. Nominal composition of alloys

Alloy Designation	Atomic Percent			Weight Percent		
	Sn	Hf or Ti	Mg	Sn	Hf or Ti	Mg
T5	1.1	0	98.9	5.15	0	94.85
T5-0.8Hf	1.1	0.11	98.79	5.12	0.77	94.11
T5-1.5Hf	1.1	0.22	98.68	5.08	1.53	93.39
T5-0.2Ti	1.1	0.11	98.79	5.15	0.21	94.64
T5-0.4Ti	1.1	0.22	98.68	5.14	0.41	94.45
T10	2.2	0	97.8	9.9	0	90.1
T10-0.7Hf	2.2	0.11	97.69	9.84	0.74	89.42
T10-1.5Hf	2.2	0.22	97.58	9.77	1.47	88.76
T10-0.2Ti	2.2	0.11	97.69	9.89	0.20	89.91
T10-0.4Ti	2.2	0.22	97.58	9.88	0.40	89.72

Figure 3.1. Furnace used for casting alloys under controlled atmosphere

Figure 3.2. Custom-made vacuum set-up for encapsulation

Artificial Ageing

After homogenization, age hardening behavior of the samples was studied by artificial ageing in Silicone oil bath at 200 °C. Vickers hardness of the samples was measured at certain time intervals by a Wilson Tukon 200 hardness tester under 1000 grams of load applied for 15 seconds. At least six measurements were done and the average is reported at each point.

Metallographic Sample Preparation

For microstructural studies, samples were mechanically ground with 600 and 1200 SiC papers using ethanol/glycerol mixture as grinding media. Samples were then polished by alumina particles down to 0.03 microns. After polishing, they were etched in Nital solution (5 vol.% Nitric acid in Ethanol) in order to reveal grain boundaries.

Instrumental Characterization

Scanning Electron Microscopy (SEM)

A JEOL JSM-6330F Field Emission Scanning Electron Microscopy (FEG-SEM) equipped with Energy Dispersive Spectroscopy (EDS) was used to study the microstructure of the samples. Accelerating voltage was 20 kV. Secondary electron images were used to study the microstructure of the samples in as cast and peak aged conditions.

X-ray Diffraction Analysis (XRD)

X-ray diffraction analysis was carried out by a Siemens 500D X-ray Diffractometer (XRD) at 40 kV and 40 mA using Cu-Kα (λ = 1.542 Å) radiation. The step size was set to 0.02° and the scan rate to 0.5° per minute. Data were acquired for 2θ range of 10° to 90°. By comparison of JCPDS cards and observed peaks, the phases present in each sample were determined. The following cards from the database were used as a reference for the analysis:

Mg: JCPDS PDF No. 035-0821

Sn: JCPDS PDF No. 004-0673

Hf: JCPDS PDF No. 038-1478

Ti: JCPDS PDF No. 044-1294

Mg_2Sn: JCPDS PDF No. 007-0274

Transmission Electron Microscopy (TEM)

A JEOL JIB-4500 Multi-beam Focused Ion Beam equipped with a Gallium ion gun was used to mill out thin foils of the samples for TEM analysis. TEM was done by a Phillips CM-200 operating at 200 kV. Three different areas of the samples were used to calculate the number density of the precipitates in unit volume.

For high resolution TEM (HRTEM), HAADF TEM characterization was carried out using a FEI/Tecnai™ F30 300 kV TEM equipped with a Fischione™ high angle annular dark field (HAADF) detector and an energy dispersive x-ray (EDX) detector. In situ lift out (INLO) technique was employed to obtain site-specific TEM thin foils by using a FEITM TEM200 Focused Ion Beam (FIB) with Gallium ion source.

Nano-mechanical Testing

Nano-indentation measurement was performed using a Hysitron TI-900 (Hysitron Inc., Minneapolis, MN, USA) Triboindenter with a Berkovich diamond tip (tip radius: 100 nm). Tip area calibration was performed on a standard fused quartz sample of known hardness (H=9.25 GPa) and modulus (E=69.6 GPa). Normal load was applied to the sample surface to a peak load of 10 mN in 5 seconds. After keeping the sample under the load for a certain holding time, the unloading was performed in 5 seconds. Varying holding times of 60, 120, 180, 240, 300 and 360 seconds were used nano-indentation creep tests.

4. Results and Discussion

Ageing Response

Age hardening behavior of the alloys at 200 °C are illustrated in Figure 4.1 to 4.4. A summary of ageing response of the samples is also presented in Tables 4.1 and 4.2 for easier comparison. In looking at these data, three important features can be noted:

First, initial hardness of all microalloyed compositions is either equal to or lower than the hardness of binary Mg-Sn alloys. This shows that the observed increase in peak hardness is not due to the addition of a harder alloying element to the compositions (i.e. Ti or Hf). Otherwise, one would expect to see some increase in the initial hardness of the microalloyed compositions as well.

Table 4.1. Ageing response of T5 and microalloyed compositions

Alloy composition	Time to reach peak hardness (h)	Initial hardness (VHN)	Max. Hardness (VHN)	Max. Increment in hardness (VHN)	Percent increase in hardness
T5	900	37.4 ± 3.7	44.5 ± 0.6	7.1	19.0
T5-0.2Ti	77	35.3 ± 3.8	47.9 ± 3.6	12.6	35.7
T5-0.8Hf	77	37.1 ± 3.8	47.7 ± 1.0	10.6	28.6
T5-0.4Ti	77	33.5 ± 1.4	45.2 ± 2.5	11.7	34.9
T5-1.5Hf	77	32.7 ± 1.9	44.9 ± 1.5	12.2	37.3

Secondly, the percent increase in hardness and increment in hardness were both improved by Hf or Ti additions. Addition of 0.1 at.% Hf improves the percent increase in hardness from a mere 19% to 28.6% in T5-0.8Hf. This increase is even more in T5-

0.2Ti, T5-0.4Ti, and T5-1.5Hf samples reaching to 35.7%, 34.9% and 37.3% respectively. This shows an almost a two-fold increase over the binary T5 alloy.

The percent increase in hardness in modified T10 alloys are also improved. Hf additions lead to an increase in hardening response from 35.4% to 41.8% and 44.9% in T10-0.7Hf and T10-1.5Hf respectively. Modifying with Ti also increases the hardening response from 35.4% to 39.6% and 46.5% in T10-0.2Ti and T10-0.4Ti respectively. The observed improvement in precipitate formation kinetics is in good agreement with previous studies [1,2], where micro-alloying with Na decreased time to reach peak hardness in the same manner. Microalloying results in formation of more nucleation centers and therefore refines the precipitate size, which in turn improves hardening response upon ageing.

Table 4.2. Ageing response of T10 and microalloyed compositions

Alloy composition	Time to reach peak hardness (h)	Initial hardness (VHN)	Max. Hardness (VHN)	Max. Increment in hardness (VHN)	Percent increase in hardness
T10	220	39.8 ± 4.2	53.9 ± 2.2	14.1	35.4
T10-0.2Ti	49	40.2 ± 3.0	56.3 ± 3.0	15.9	39.6
T10-0.7Hf	49	40.2 ± 2.5	57 ± 2.4	16.8	41.8
T10-0.4Ti	49	40.4 ± 4.1	59.2 ± 3.5	18.8	46.5
T10-1.5Hf	96	40.1 ± 2.3	58.1 ± 1.5	18.0	44.9

Thirdly and most importantly, time to reach peak hardness is significantly reduced by microalloying. The sluggish precipitate formation process in T5 was expedited by an order of magnitude, reducing from about 900 hours to 77 hours in all of the four modified compositions.

There is a substantial decrease in time to reach peak hardness in T10 alloys, too. Peak hardness occurs after 220 hours of aging in T10 binary alloy, which is reduced to 49 in

three of the four modified compositions. This shows more than a four fold decrease in time to reach peak hardness. Time to reach peak in T10-1.5Hf shows a two fold improvement. The main reason behind observed improvement is formation of additional nucleation centers, which is confirmed by TEM results presented in future sections.

Finally, it is also interesting that binary alloys, especially T5, are more prone to over-ageing. Hardness of microalloyed compositions declines with a slower rate as compared to T5 and T10. It has been suggested that the presence of microalloying element at the interface of precipitates and matrix reduces interfacial energy and hinders precipitate coarsening due to over-ageing [3]. Based on the results of the age hardening experiment, T5 modified samples were chosen for further analysis.

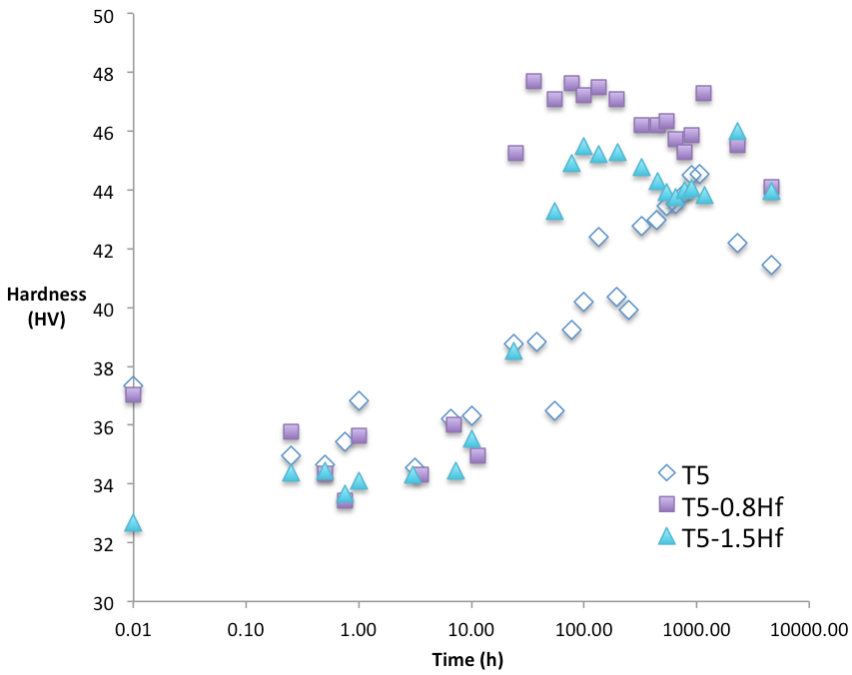

Figure 4.1. Age hardening response of T5 and Hf modified alloys

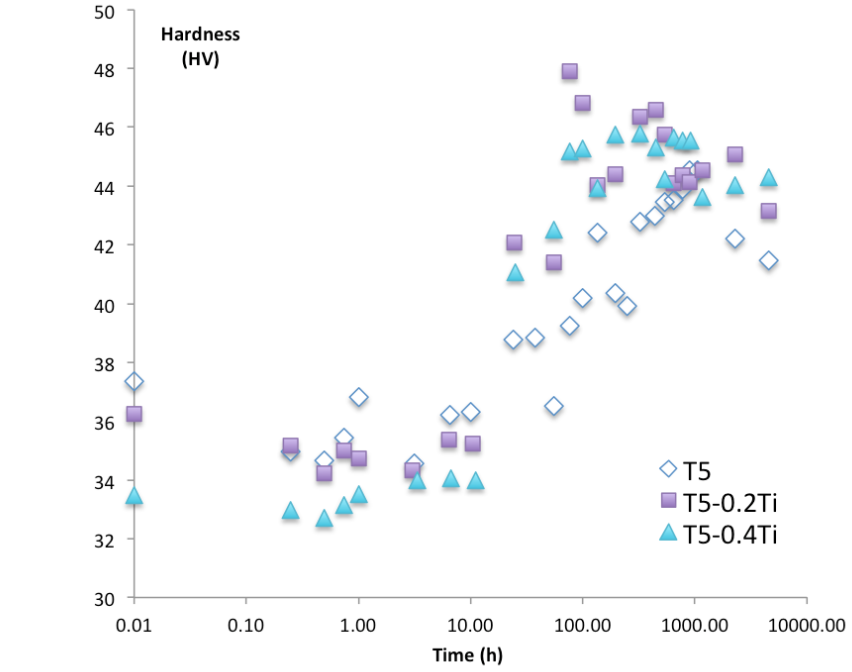

Figure 4.2. Age hardening response of T5 and Ti modified alloys

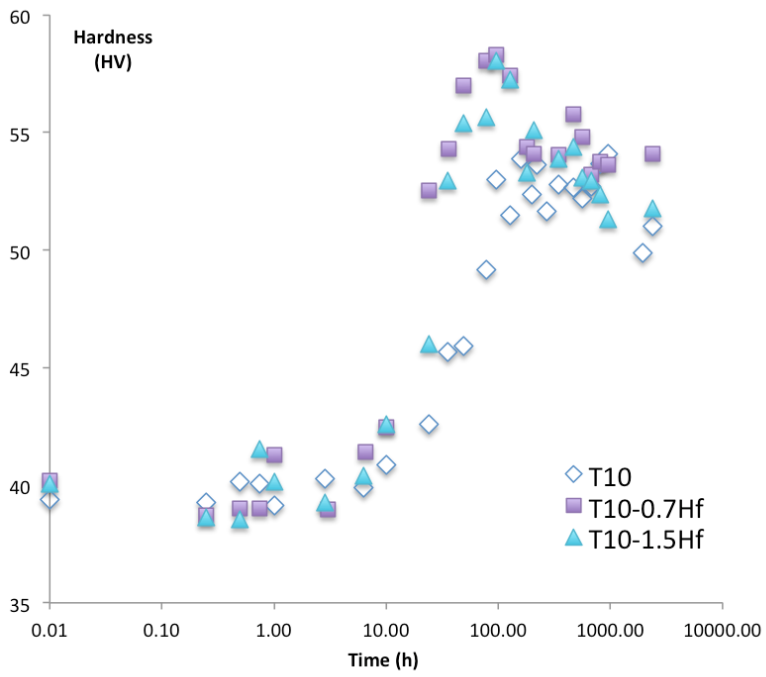

Figure 4.3. Age hardening response of T10 and Hf modified alloys

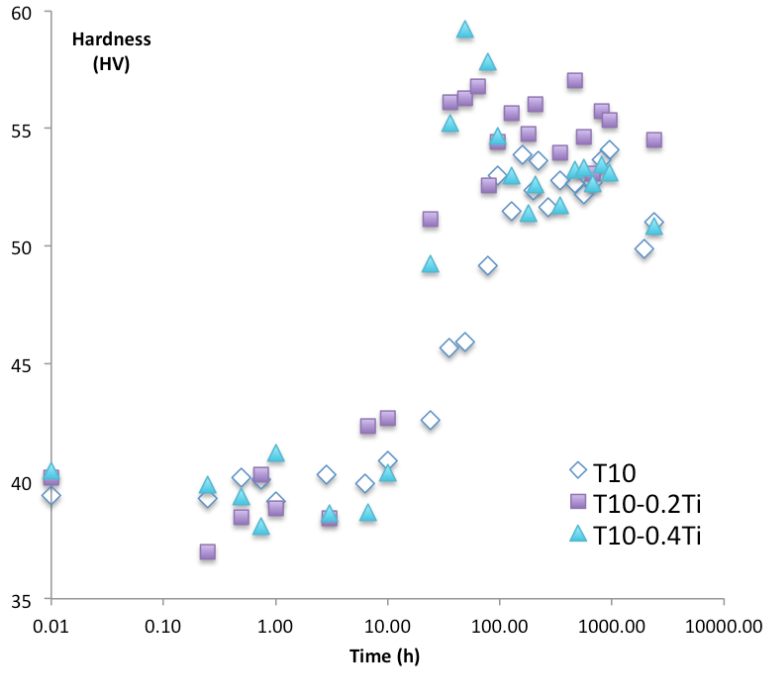

Figure 4.4. Age hardening response of T10 and Ti modified alloys

Microstructural Analysis

Grain Size Analysis

For microstructural studies, samples were polished and etched to reveal grain boundaries. Figures 4.5 and 4.6 show the optical micrographs of microstructure of T5 at 77 hours, and microalloyed compositions at peak hardness. According to Heyn Lineal Intercept method (ASTM E112-96), several lines in different orientations were drawn on three pictures of each sample and the average grain size was measured. The results are shown in Table 4.3 below.

Table 4.3. Grain Size Analysis

Alloy composition	Average Grain Size (μm)	Standard Deviation (μm)
T5	231.4	91.0
T5-0.2Ti	170.0	56.3
T5-0.8Hf	211.1	74.7
T5-0.4Ti	354.2	161.3
T5-1.5Hf	367.0	139.4

T5-0.2Ti shows a 27% refinement in grain size. In contrary, a significant grain coarsening effect (53% increase) is observed in T5-0.4Ti. Comparison of as cast microstructure of Ti modified alloys shown in Figure 4.7 demonstrates that same trend exists in the as cast state. Addition of 0.2 Ti to T5 alloy, refines the microstructure and increases the number of secondary dendrite arms. Upon further addition of Ti, not only the number of the secondary dendrite arms decreases but also the grain size increases as well.

In case of Hf, low alloy content sample shows only 10% decrease in average grain size, which is negligible when compared to the standard deviation; but similar to Ti, grain size in T5-1.5Hf sample is increased by 59% by further addition of Hf. Microstructure of as cast Hf modified samples is shown in Figure 4.8. In T5-1.5Hf sample, long columnar

grains are observed which are not seen in T5 or T5-0.8Hf samples. Therefore, it can be concluded that differences in grain structure of the samples exist right after the casting and did not initiate during the ageing.

Previous studies have reported grain refinement in Mg alloys by Ti addition, nevertheless no specific mechanism was reported for these effects [4,5]. Unlike Aluminum, a universally reliable grain refiner system is not available for Magnesium alloys. In most cases, grain refinement depends on the chemistry of the alloy system [6,7].

As no evidence of presence of new intermetallics at the grain boundaries was found in other microstructural analysis, the differences in grain structure must have been originated in primary nucleation stage. Addition of potent nucleating particles can lead to grain refinement. But it is well established only a small percentage (1-2%) of these inoculates contribute to the nucleation of the grains. Greer proposed Free Growth Theory in an effort to justify why only such small proportions of these inoculants affect grain nucleation [8,9]. According to this theory, grain initiation is determined by the barriers to growth of nuclei rather than the nucleation event itself. This barrier is controlled by the linear dimension of the inoculants. Bigger particles have the highest potency for nucleation. Grain formation starts on these particles and continues gradually to smaller inoculants if any. The difference observed between Ti and Hf containing samples in terms of grain refinement may be due to the fact that the particle size of the Ti powder was bigger than Hf powder used for making alloys.

Grain coarsening effects seen by further addition of microalloying element may be justified in the light of Interdependence Theory of grain refinement [10]. Interdependence Theory attempts to look at nucleation and growth as concurring events that affect grain size distribution whereas traditional theories formulate the two as independent stages.

This theory has been applied to a number of experimental data on Aluminum and Magnesium alloys and can successfully predict as-cast grain size.

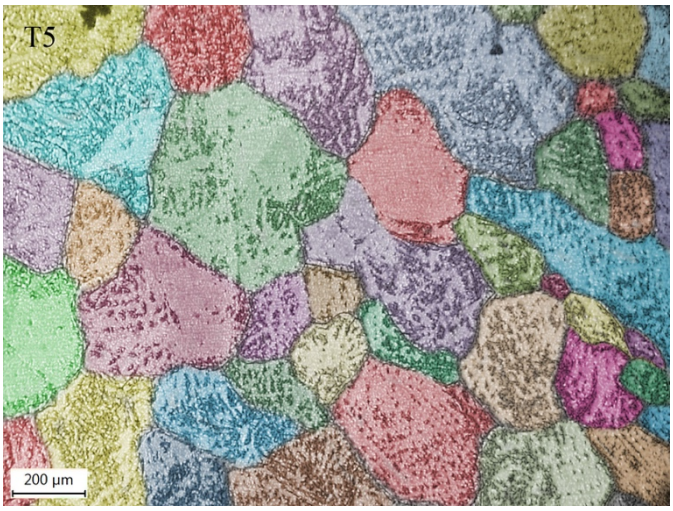

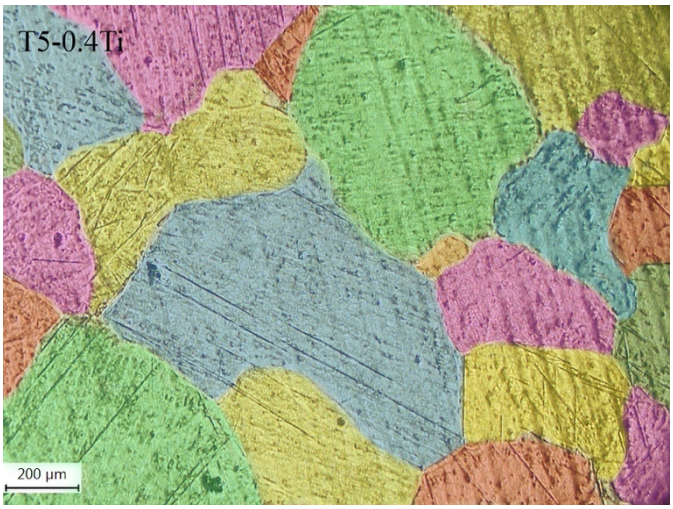

Figure 4.5. Optical micrographs of grains in T5 and Ti modified peak aged alloys

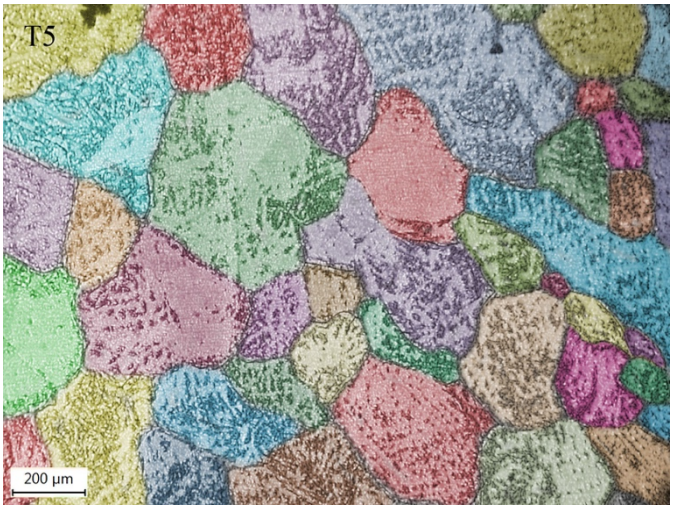

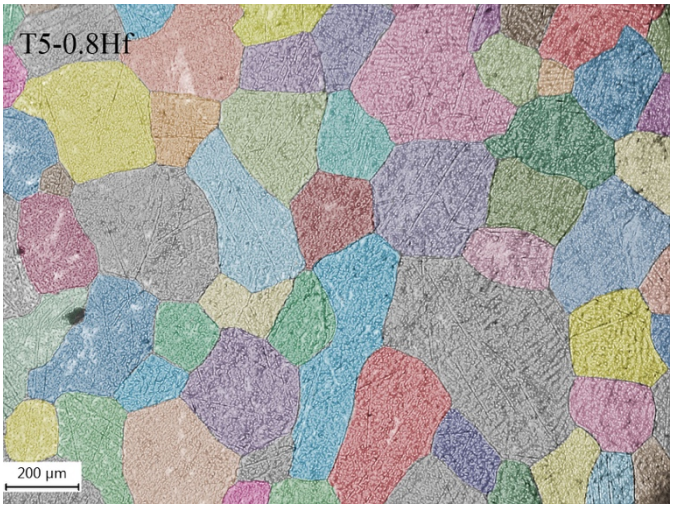

Figure 4.6. Optical micrographs of grains in T5 and Hf modified peak aged alloys

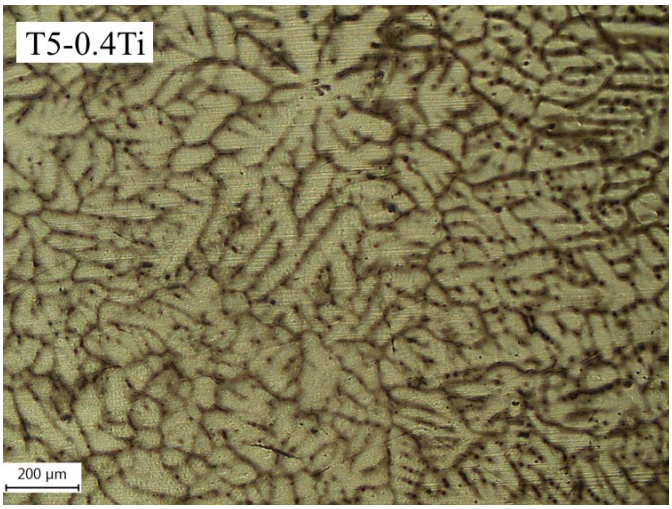

Figure 4.7. Optical microscopy images of T5 and Ti modified as cast alloys

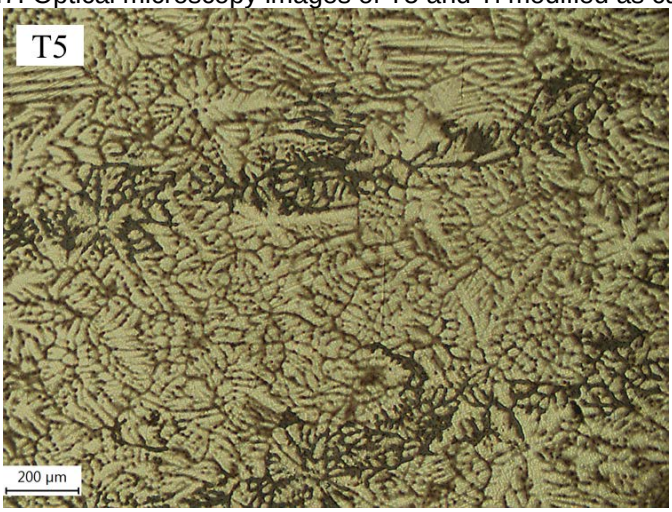

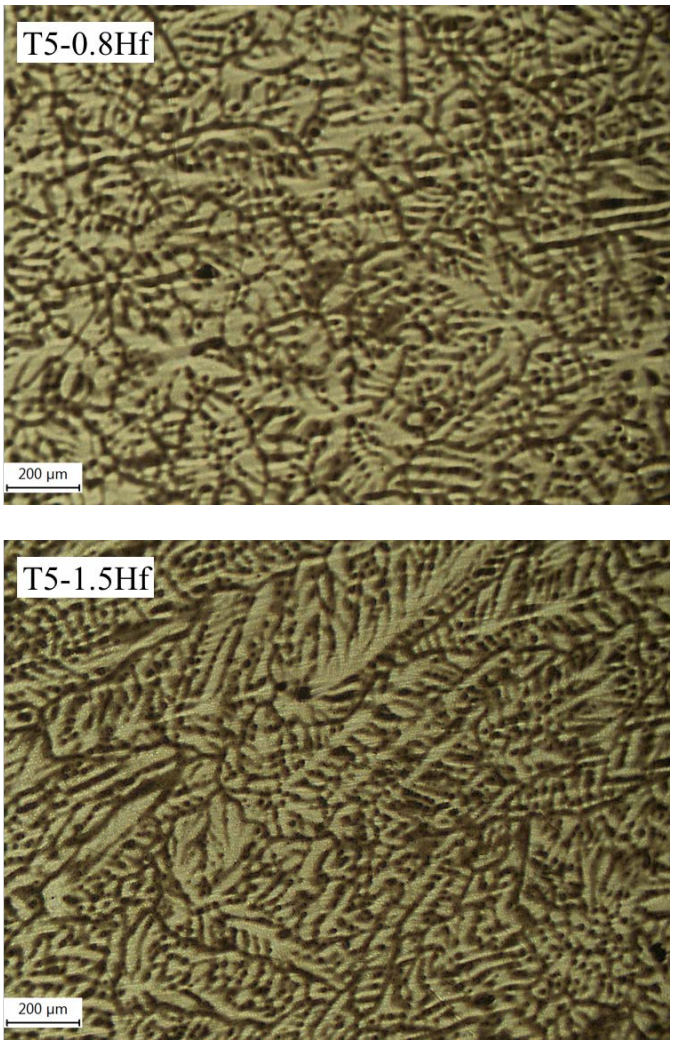

Figure 4.8. Optical microscopy images of T5 and Hf modified as cast alloys

According to this theory, the final grain size is controlled by three critical distances:

1. The distance that a formerly nucleated grain must grow to create enough constitutional supercooling ahead of solid-liquid interface so that the nucleation of the next grain can be started. This means that there is a nucleation free zone around each nucleate inside which no new nucleation can happen until critical undercooling is generated. 2. The distance between solid-liquid interface and the point at which this critical constitutional supercooling has been produced; and 3. The extra distance to the

closest most potent nucleant. If the undercooling for nucleation (ΔT_n) is less than 6 °C, then the model shows:

$$\Delta T_n = 4\sigma / (\Delta S_v d) \qquad \text{Equation 4.1.}$$

Where d is nucleant particle diameter, ΔS_v is the entropy of fusion, and σ is the solid-liquid interfacial energy. Figure 4.9 shows the relationship between ΔT_n and particle diameter (d) and average particle spacing S_d when ΔT_n < 0.8 °C. These particles are most likely to act as operative nucleants. As can be seen, when the particle spacing becomes less than 20 μm, there is a drastic increase in ΔT_n .

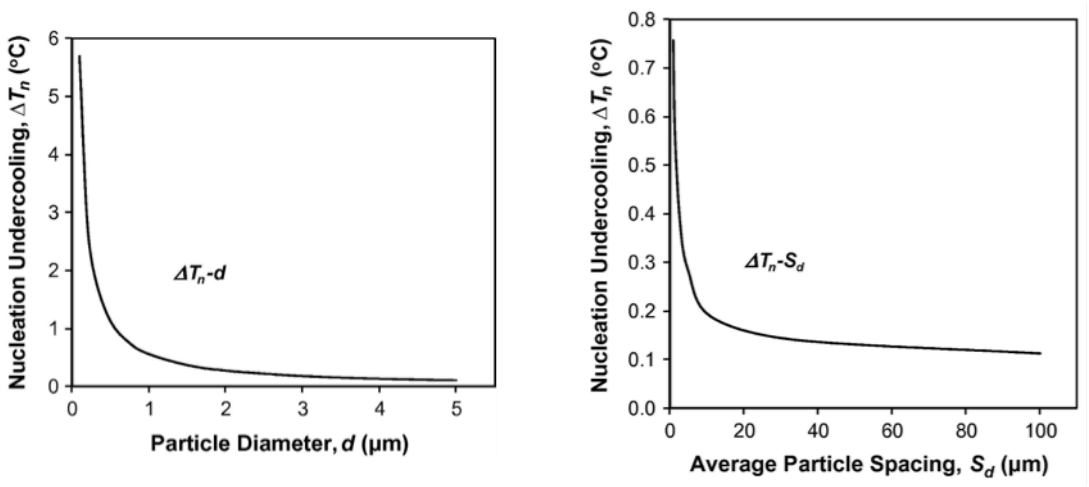

Figure 4.9. Relationship between constitutional undercooling and nucleant particle characteristics as predicted by interdependence theory [10]

This means there is a higher possibility for new nucleation events to start at farther distances from previously nucleated grains. Considering the fact that both Hf and Ti have very limited solubility in Mg and both have a tendency to segregate, when more Hf or Ti is added to the melt, there is a higher chance that inter-particle spacing falls in the range that requires a much higher nucleation undercooling. Therefore, these particles

won’t be able to act as potent nucleants. This may be the reason for grain coarsening observed in T5-0.8Hf and T5.0.4Ti alloys.

Scanning Electron Microscopy (SEM/EDS)

Elemental maps for microalloyed samples are shown in Figures 4.10 to 4.13. As can be seen microalloying element is randomly distributed in all of the samples. Semi-quantitative compositional analysis was also performed by doing EDS at multiple locations of each sample to verify the compositions. Summary of these results are presented in Table 4.4 below.

Table 4.4. Composition analysis by EDS

Nominal Alloy Composition (at.%)	Mg (at.%)	Sn (at.%)	Hf/Ti (at.%)
Mg-1.1Sn (T5)	98.65 ± 0.23	1.35 ± 0.23	NA
Mg-1.1Sn-0.11Ti (T5-0.2Ti)	98.66 ± 0.13	1.25 ± 0.07	0.09 ± 0.10
Mg-1.1Sn-0.11Hf (T5-0.8Hf)	98.43 ± 0.13	1.48 ± 0.17	0.09 ± 0.07
Mg-1.1Sn-0.22Ti (T5-0.4Ti)	98.51 ± 0.24	1.38 ± 0.22	0.11 ± 0.06
Mg-1.1Sn-0.22Hf (T5-1.5Hf)	98.52 ± 0.22	1.36 ± 0.22	0.12 ± 0.06

Based on these results, actual compositions are slightly richer in Sn than nominal compositions. There was some Mg loss during casting due to high vapor pressure of Mg. Concentrations measured for Ti/Hf are of little practical importance because point to point variation was too high. This is evident from comparison of standard deviations with averages of measurements especially in T5-0.2Ti and T5-0.8Hf. Because of the very low concentration of microalloying elements, it was not possible to make a more accurate measurement of their concentrations by EDS.

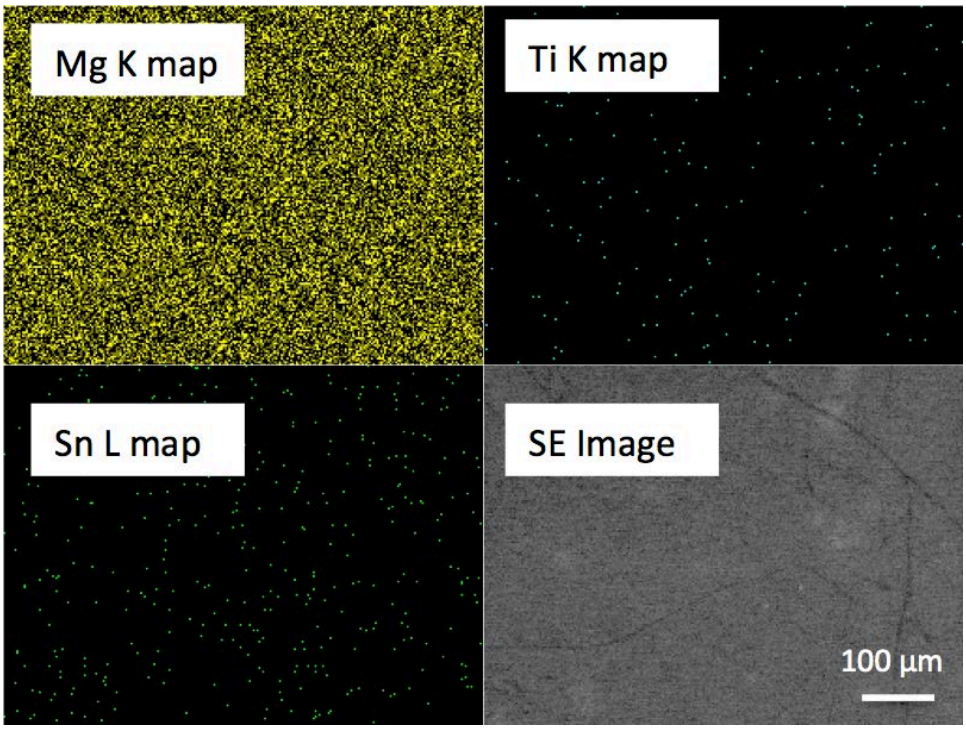

Figure 4.10. Elemental maps of peak aged T5-0.2Ti alloy

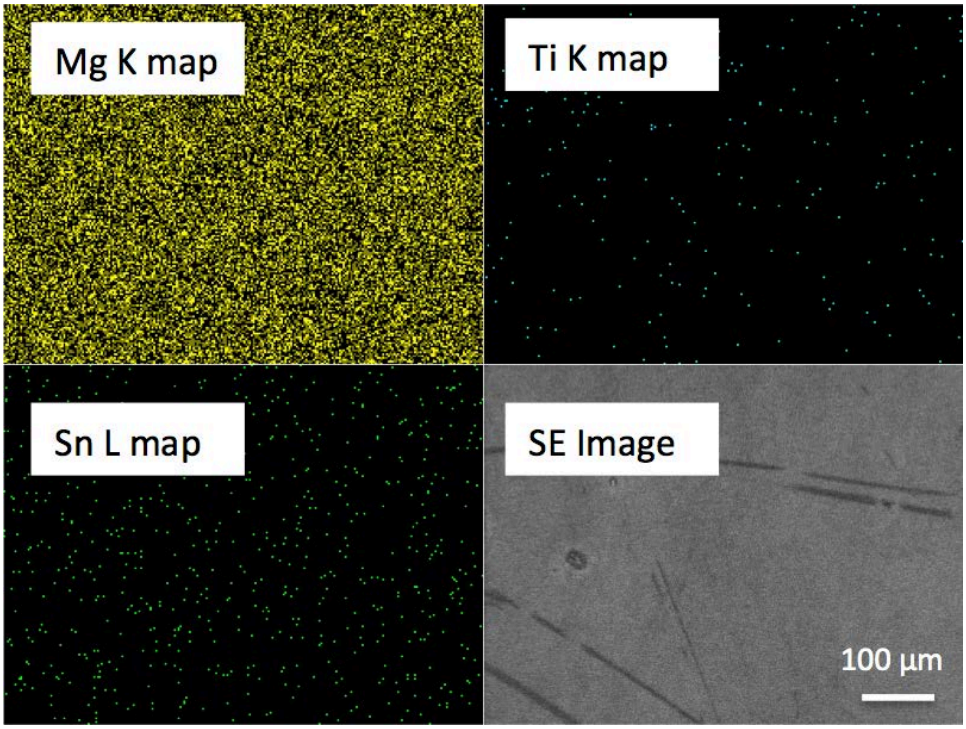

Figure 4.11. Elemental maps of peak aged T5-0.4Ti alloy

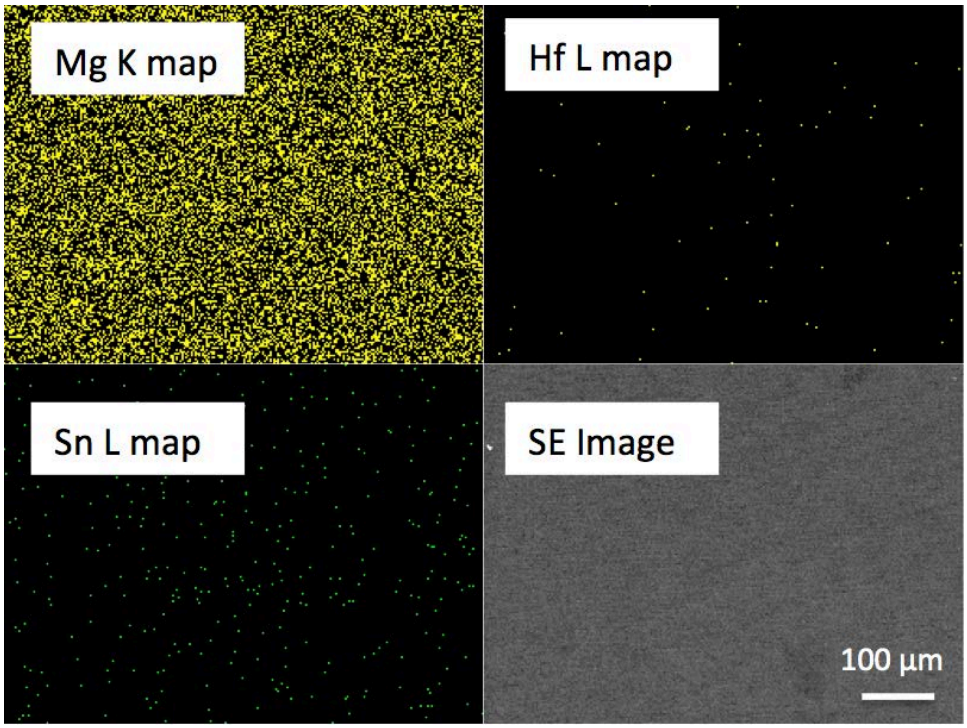

Figure 4.12. Elemental maps of peak aged T5-0.8Hf alloy

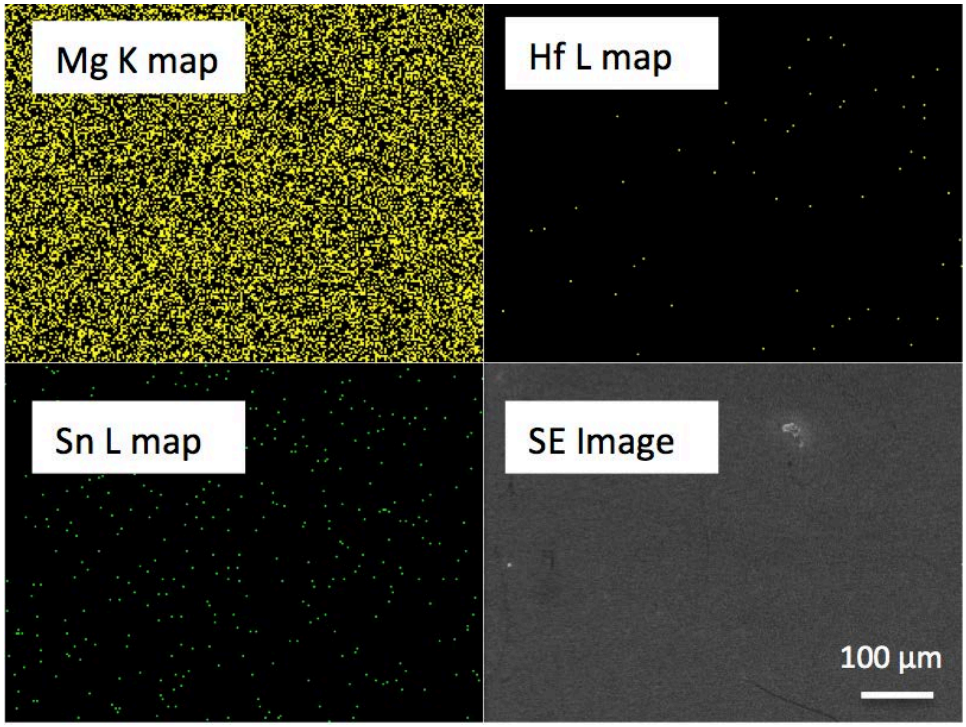

Figure 4.13. Elemental maps of peak aged T5-1.5Hf alloy

For observation of different phases, microstructures of the samples were examined by SEM at higher magnification and are shown in Figures 4.14 and 4.15. Microstructure consists of primary α-Mg matrix and Mg_2Sn particles (white particles) with lamellar eutectic at the grain boundaries. Some divorced eutectic structures were also observed at some areas of the samples.

In order to find traces of microalloying elements, EDS analysis was performed on at least 10 locations of the grain boundary and the white particles. Only Mg and Sn were detected in high magnification pictures. This is consistent with the results of X-ray diffraction analysis which are discussed in the next section.

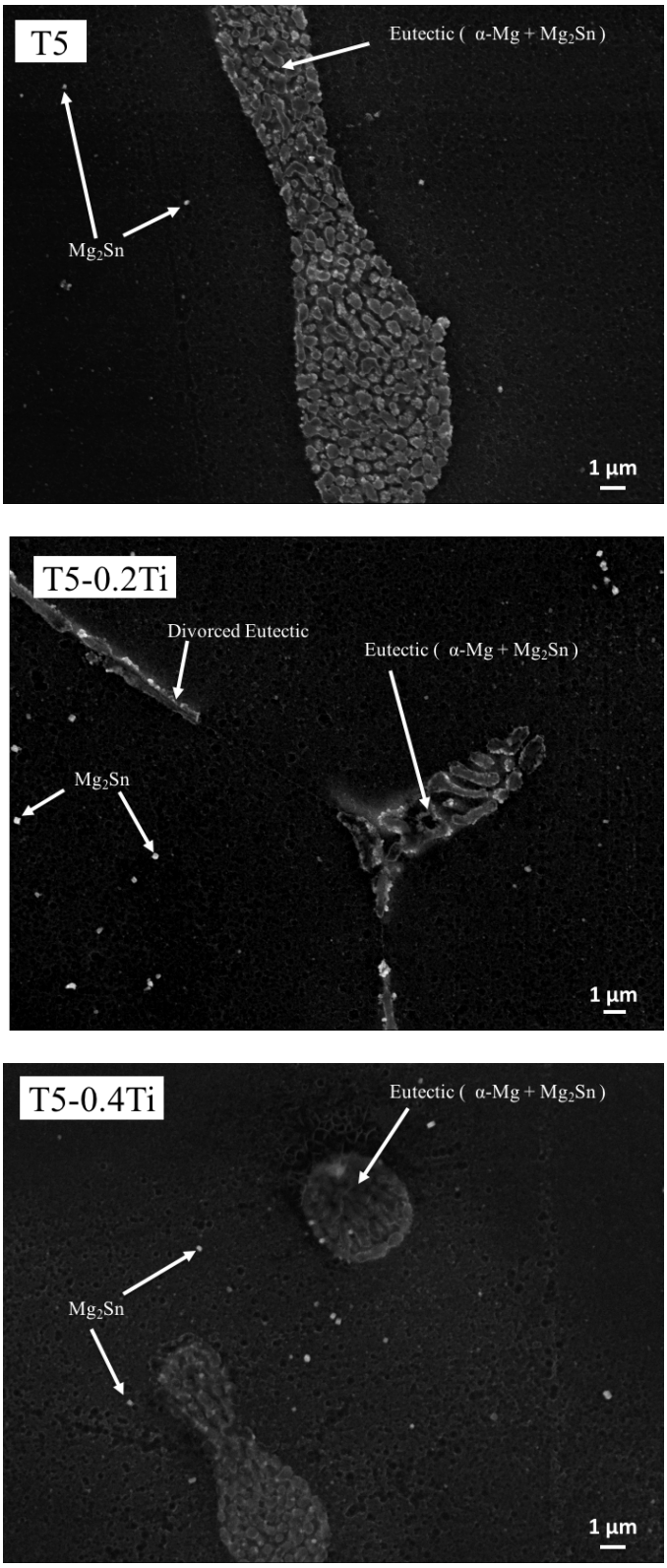

Figure 4.14. SEM images of T5 and Ti modified as cast alloys

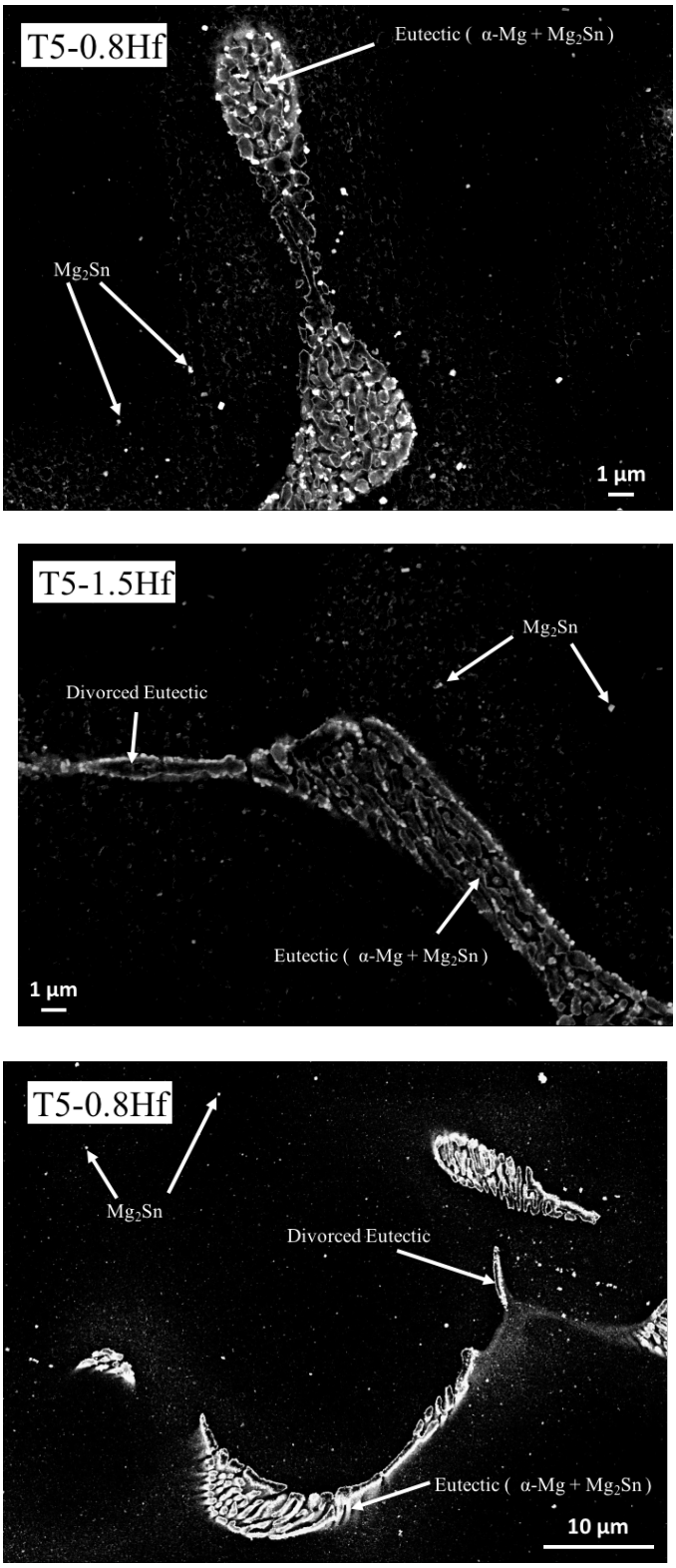

Figure 4.15. SEM images of Hf modified as cast alloys

X-ray Diffraction (XRD) Analysis

X-ray Diffraction patterns for microalloyed samples in the peak-aged and as cast conditions are shown in Figures 4.16 to 4.19 for comparison. As can be seen, all peaks can be indexed to α-Mg or Mg_2Sn. No new peaks were observed after addition of microalloying elements. Therefore, it can be concluded that no new binary or ternary intermetallics were formed after of microalloying.

Also, it is clear that peaks related to Mg_2Sn are more pronounced in the peak aged conditions, which is in agreement with previous studies [11].

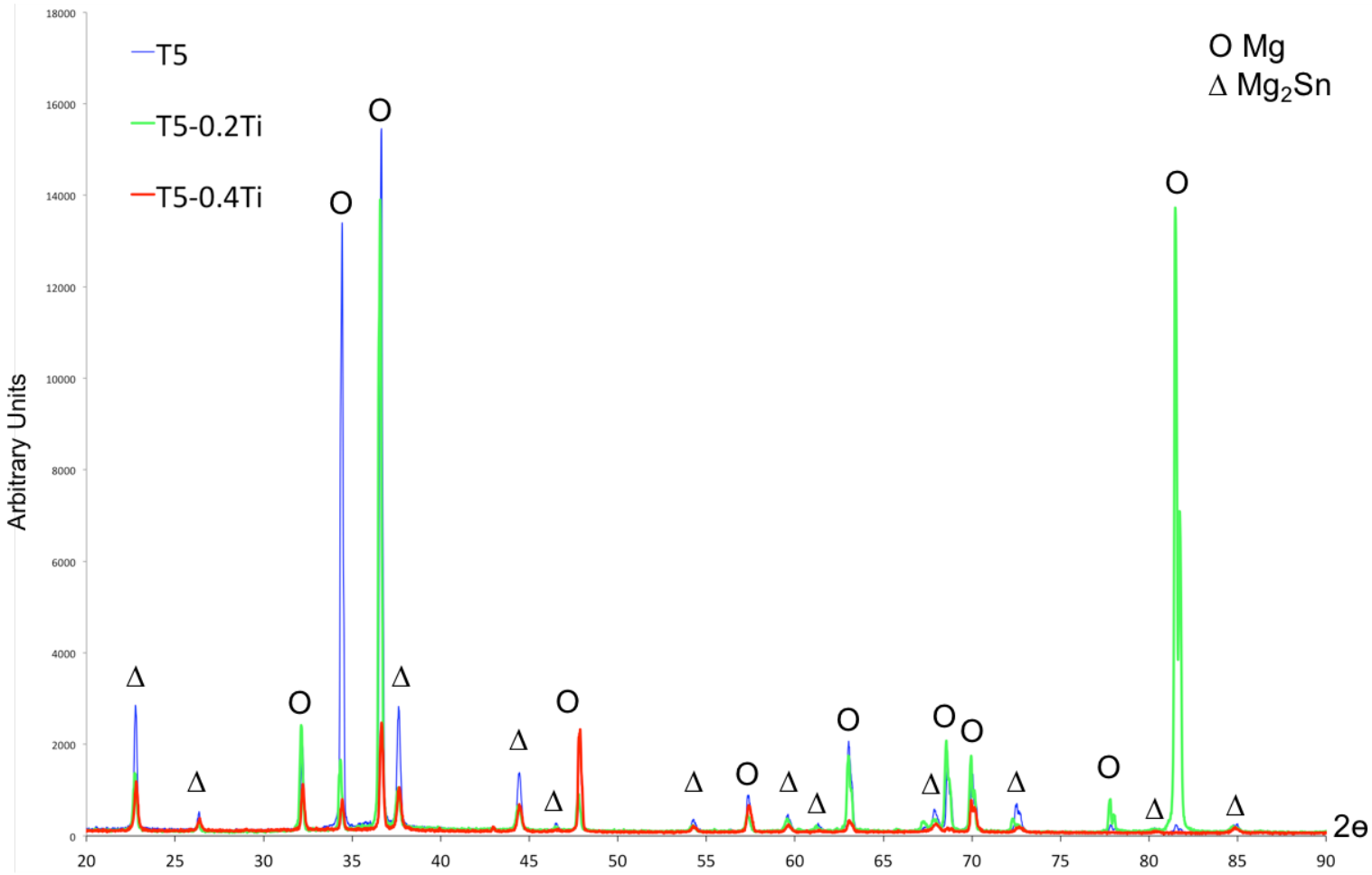

Figure 4.16. XRD patterns of T5 and Ti modified alloys at peak-aged conditions

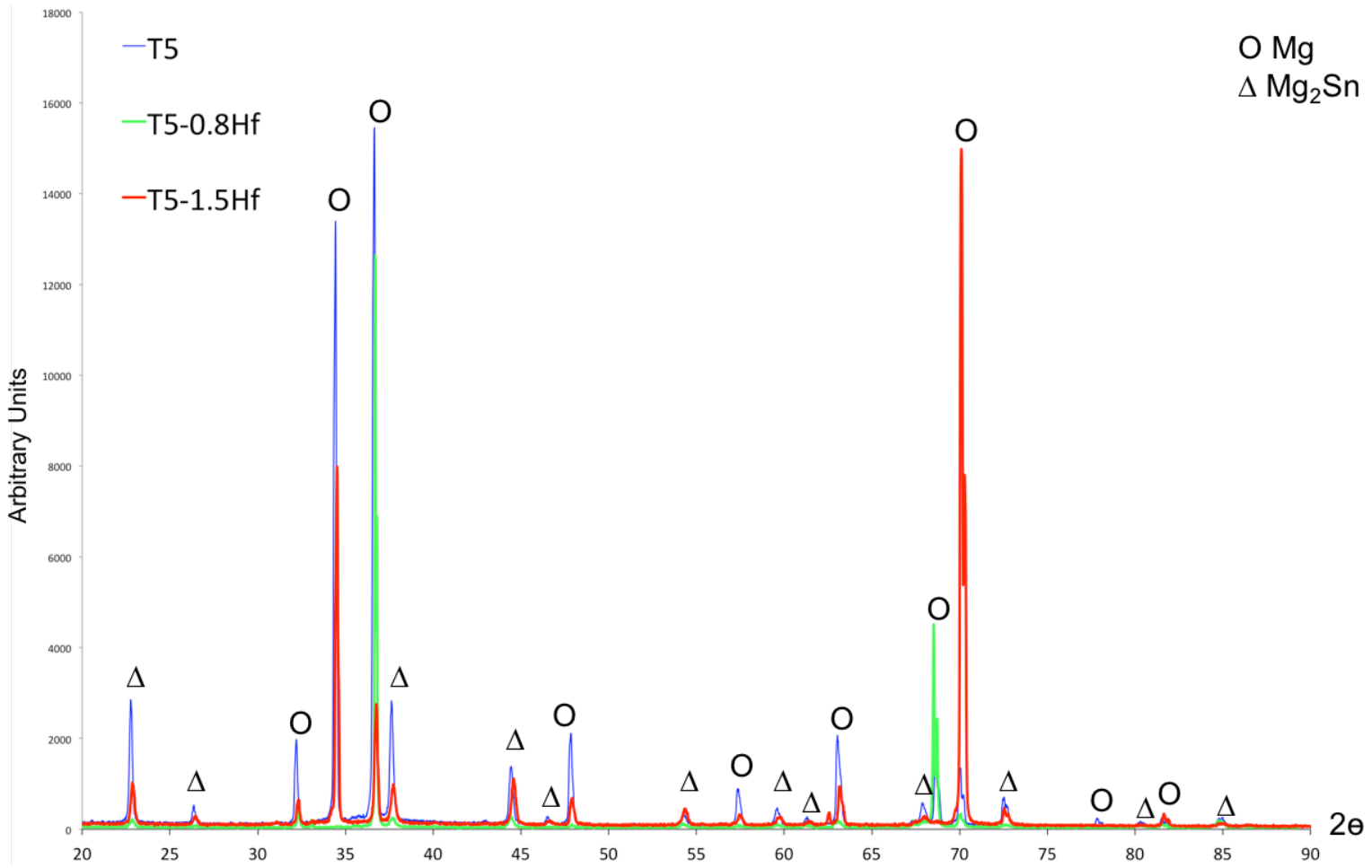

Figure 4.17. XRD patterns of T5 and Hf modified alloys at peak-aged conditions

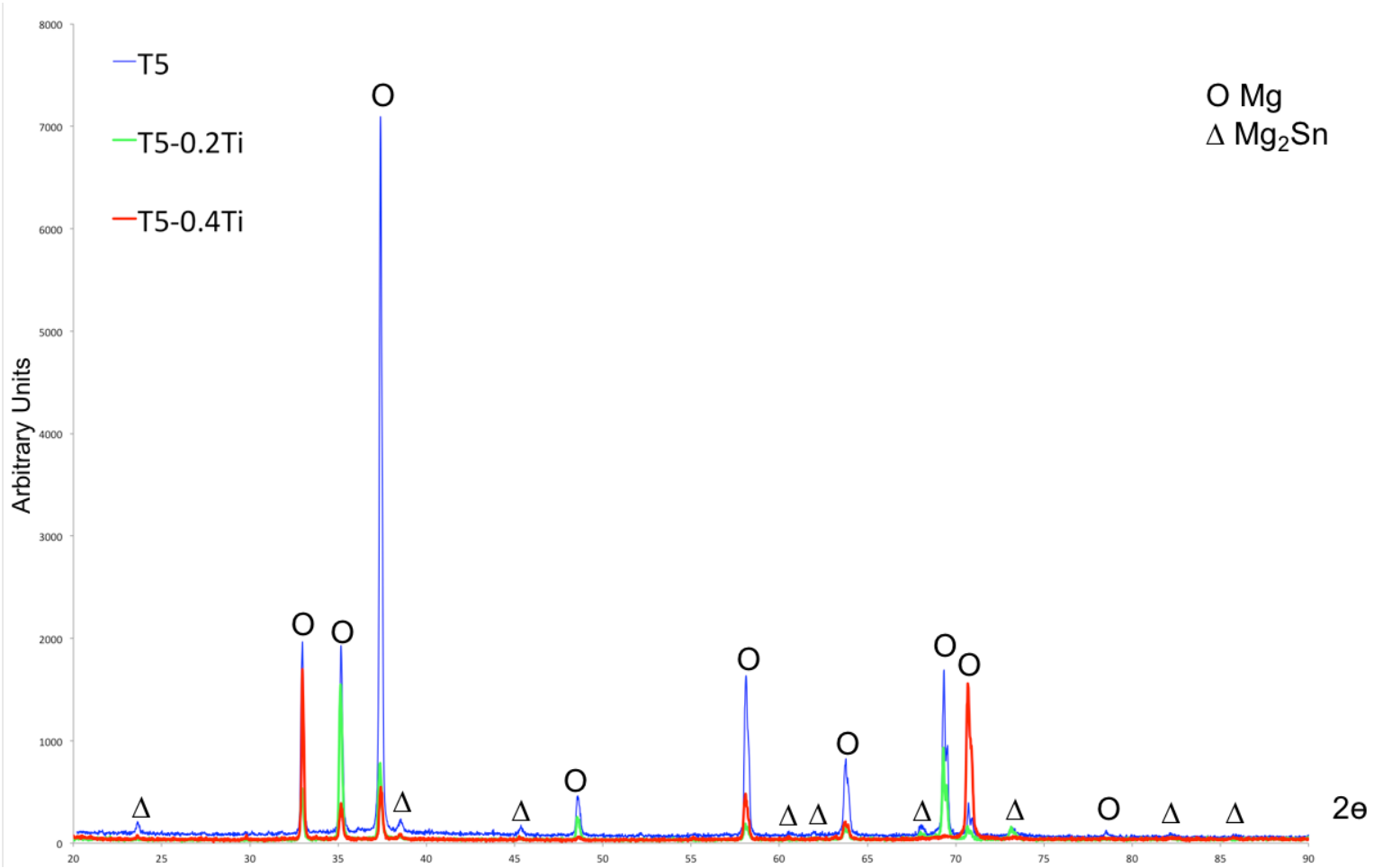

Figure 4.18. XRD patterns of as cast T5 and Ti modified alloys

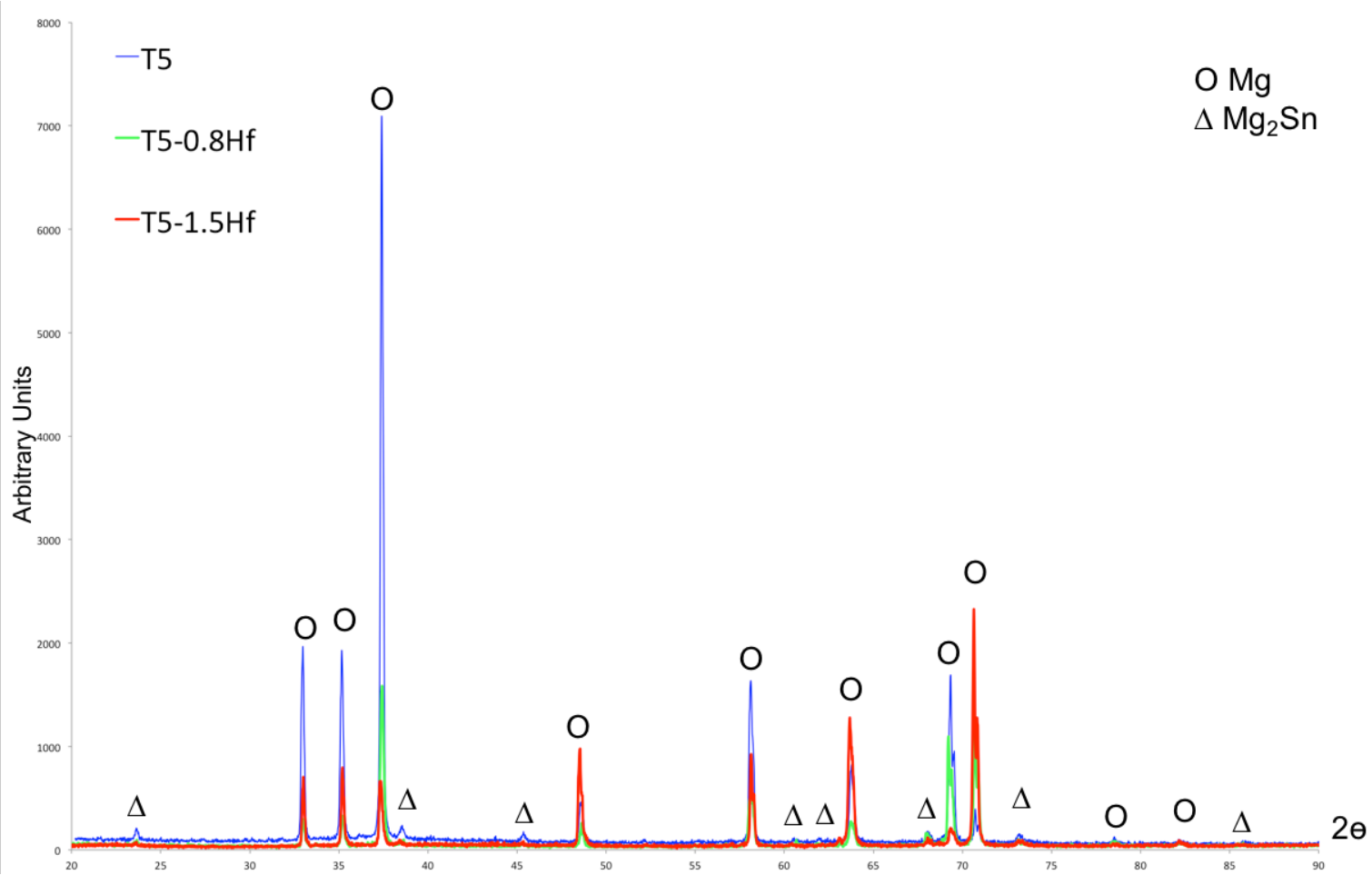

Figure 4.19. XRD patterns of as cast T5 and Hf modified alloys

Transmission Electron Microscopy (TEM)

Hafnium modified alloys were chosen for further analysis with TEM. Bright-field TEM pictures of samples are shown in Figures 4.20 and 4.21. Previous studies have reported lath shaped, plate like and polygon Mg_2Sn precipitates in Mg-Sn alloys [1,3,12-15]. In T5-0.8Hf and T5-1.5Hf, lath shaped precipitates can clearly be seen. The length of these lath-like precipitates reaches to several hundred nanometers. In T5 binary alloy, only polygon shaped precipitates of very small size (less than 20 nm) were formed in the same timescales. The aspect ratio of the precipitates is increased to 3.63 and 3.95 in T5-0.8Hf and T5-1.5Hf respectively as compared to an aspect ratio of 1.42 in T5 alloy.

Foil thickness was measured in FIB using SEM image just before welding foils to TEM grid. Thickness was measured in 5 different locations of the foil and average value was used for foil volume calculation. The length and width of the TEM image were multiplied by this thickness to calculate the volume of the foil. The dimensions and number of the precipitates were manually measured using ImageJ image analysis software in three TEM images taken from different areas of the foils for each sample. Then the number of observed precipitates was divided by calculated volume to report number volume density of precipitates. A summary of these results is presented in Table 4.6 below.

Table 4.6. Precipitate dimensions in peak-aged Hf modified alloys and T5

Alloy	N_v x 10^{18} (m^{-3})	Length (nm)	Width (nm)	L/W
T5-0.8Hf	41.20	138 ± 34	38 ± 18	3.63
T5-1.5Hf	50.40	170 ± 56	43 ± 21	3.95
T5 at 77 hours	NA	17 ± 7	12 ± 4	1.42

Number volume density of precipitates was also increased to 41.2 x 10^{18} in T5-0.8Hf and 50.4 x 10^{18} in T5-1.5Hf per m^{-3}. Previous studies on Mg-1.3Sn at.% (T6) reported a number volume density of 0.60x10^{18} per m^{-3} at its peak hardness which is two orders of magnitude lesser than the values found for Hf modified alloys in this study [1,3], which is two orders of magnitude improvement over the values reported for Mg-Sn binary alloy at its peak hardness [1,3]. Due to the small size of the precipitates in T5 alloy, we were unable to calculate number volume density of precipitates in T5 sample in low magnification pictures. Values calculated from high magnification images are not reported, because it won't be a true measure of precipitate state at bulk.

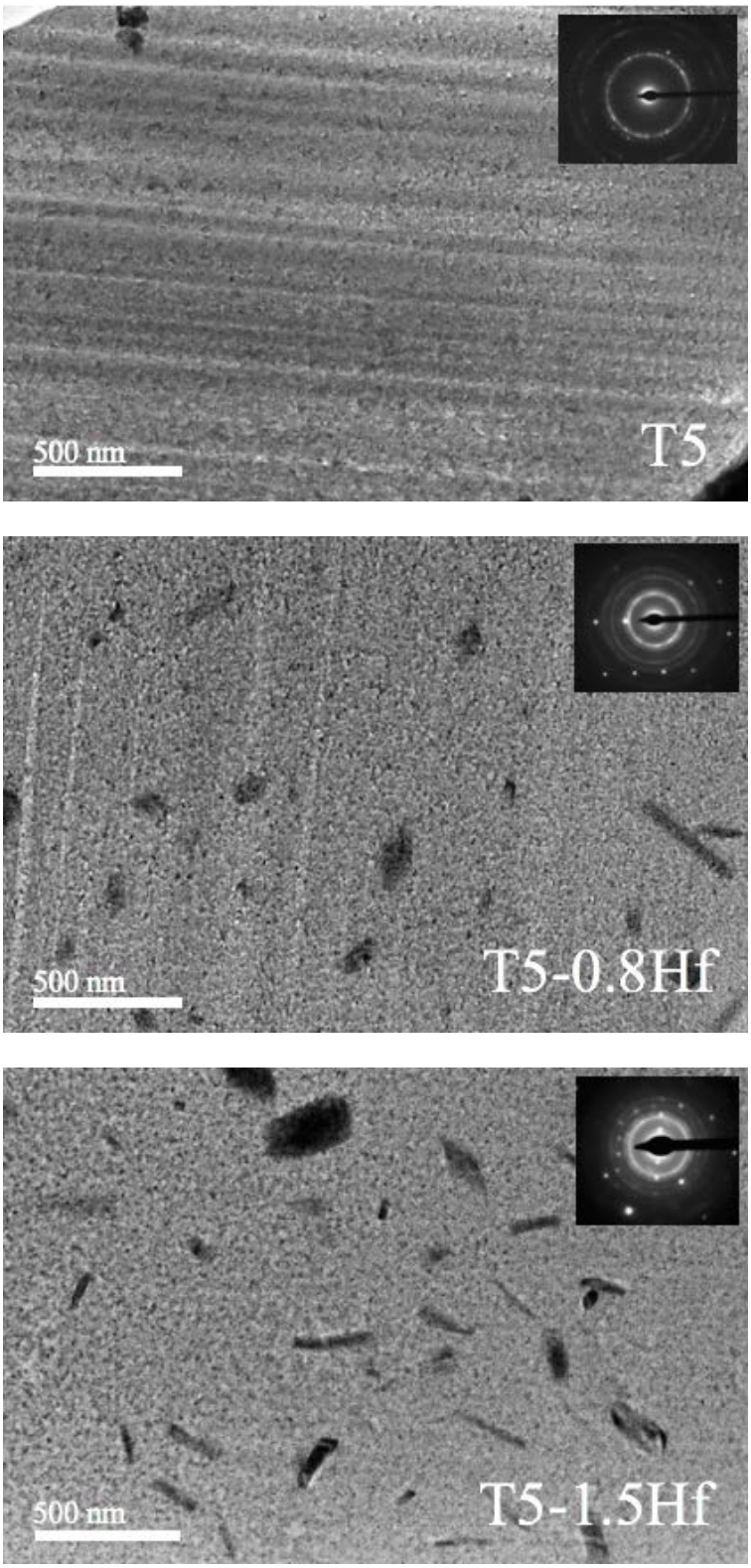

Figure 4.20. Bright-field TEM pictures of peak-aged Hf modified alloys and T5 at 77 hours of artificial aging at 200 °C

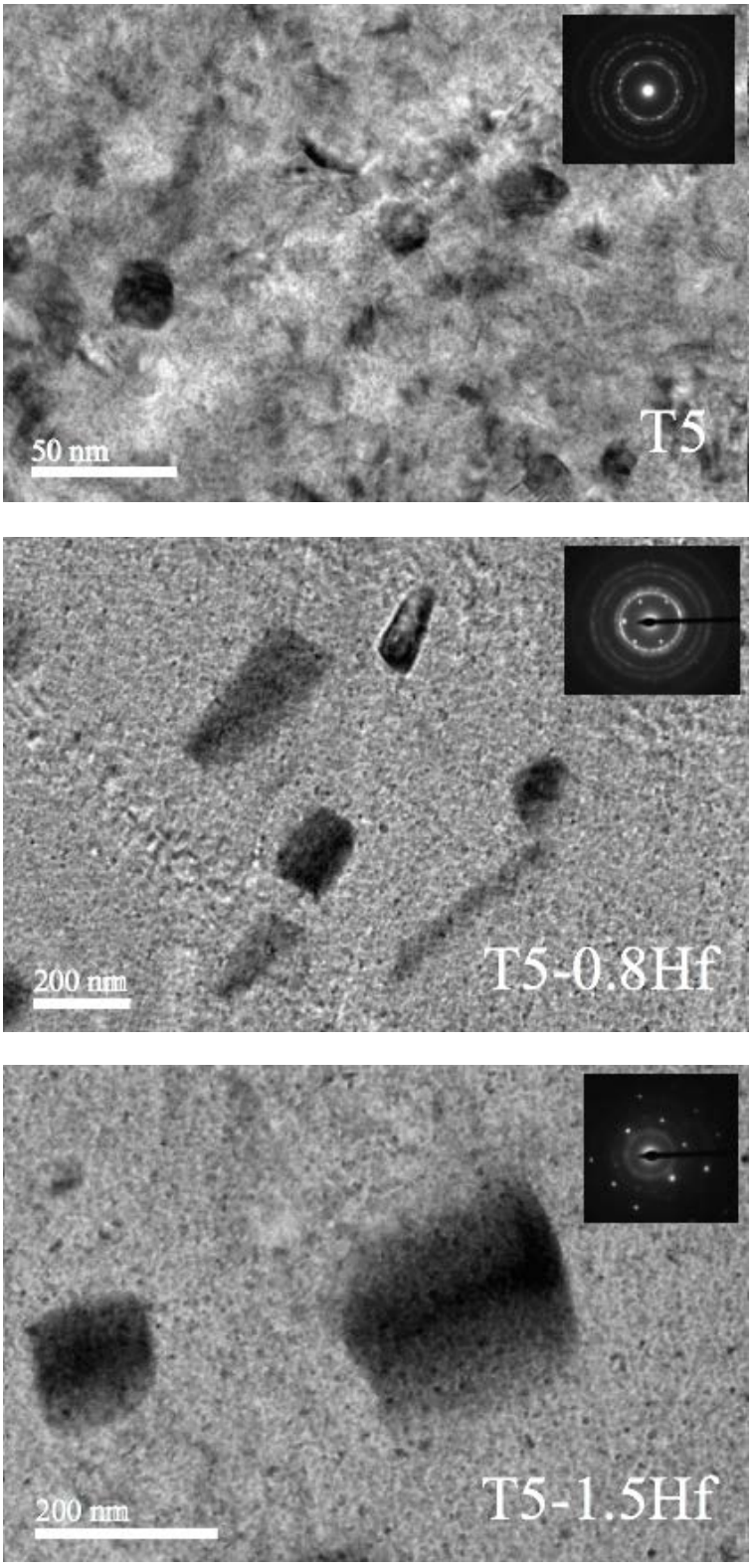

Figure 4.21. TEM micrographs of precipitates in peak-aged Hf modified alloys and T5 at 77 hours of artificial aging at 200 °C

Clusters of Hf as dark spots at the surface of the precipitates in Hf modified alloys were seen in bright field TEM images. These clusters are marked by white arrows in Figure 4.22.

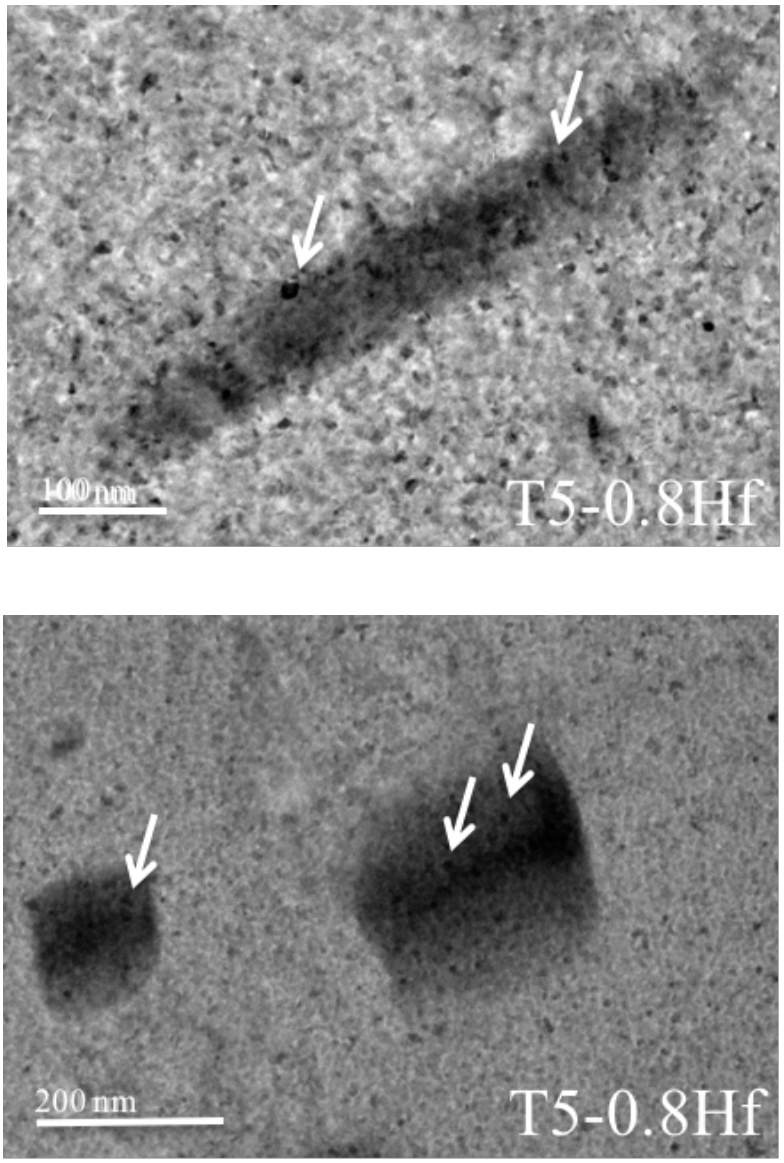

Figure 4.22. Nano-clusters of Hf at the surface of Mg_2Sn precipitates in Hf modified alloys

Selected Area Electron Diffraction (SAED) was used to verify that precipitates are in fact Mg_2Sn. Polycrystalline diffraction rings belong to Mg matrix and dots can be indexed to Mg_2Sn precipitate.

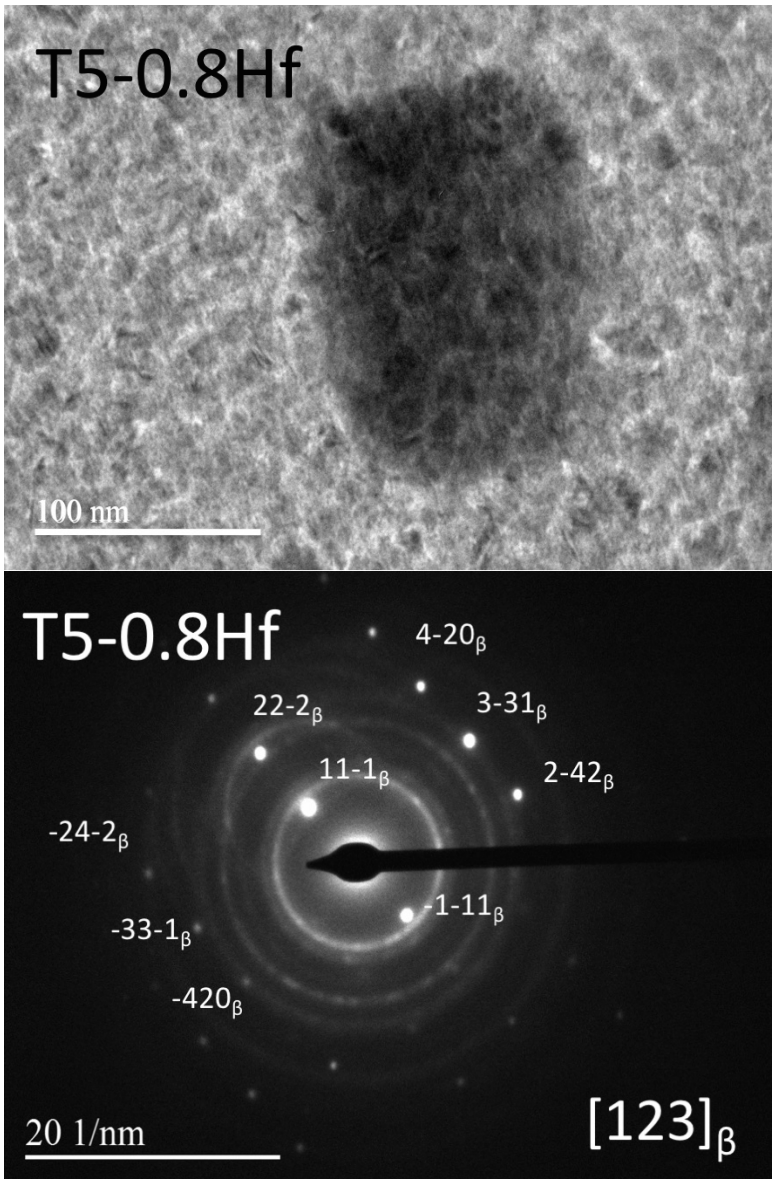

Figure 4.23. Indexed SAED pattern of Mg_2Sn precipitates in T5-0.8Hf

High-Angle Annular Dark Field (HAADF) Imaging

One of the Hafnium modified samples (T5-0.8Hf) and reference binary sample (T5) were chosen for further analysis with HAADF. Dark-field TEM pictures of samples are shown in Figures 4.24 and 4.25.

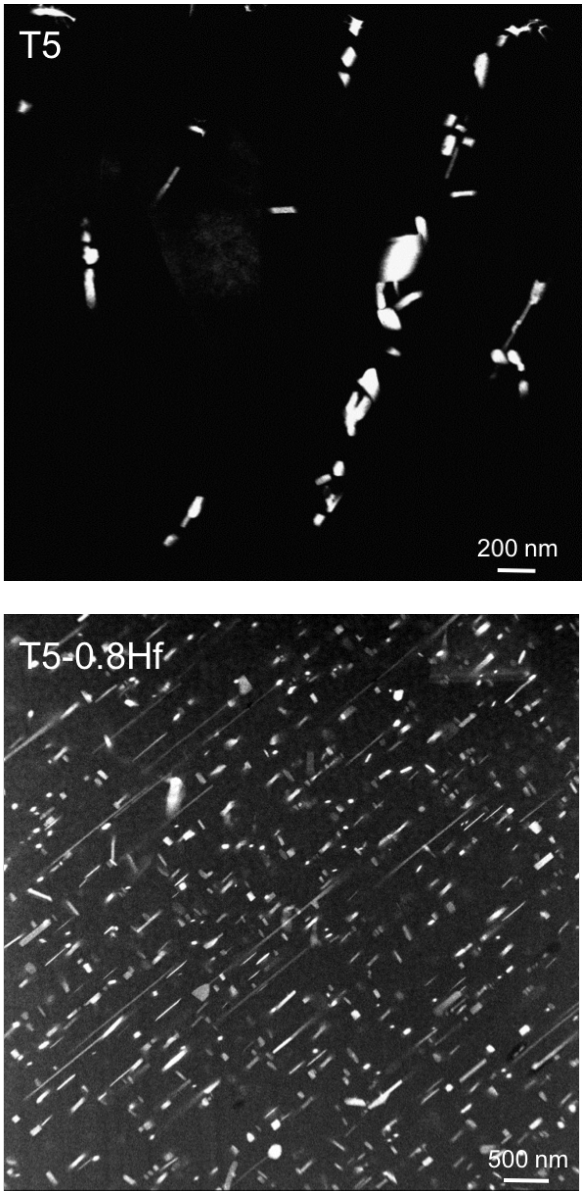

Figure 4.24. Low magnification HAADF images of T5 and T5-0.8Hf

It can be seen that there is a significant increase in number density of precipitation due to microalloying. Also, precipitates are more uniformly distributed in T5-0.8Hf sample. Energy Dispersive X-ray (EDX) spectroscopy was performed at different locations of each sample. Results are shown in Figures 4.25 and 4.26.

L-α (7.89 and 7.84 KeV) and L-β (9.02 and 9.34 KeV) lines of Hf were seen in the EDX analysis of T5-0.8Hf sample, that indicates Hf was found at the surface and areas close to precipitates. Tin L-α (3.44 KeV) and L-β (3.43 KeV) lines and Magnesium k-α (1.25 KeV) and k-β (1.30 KeV) lines can be observed in both samples. Ga peaks (k-α: 9.25 and 9.22 KeV, L-α: 1.10 KeV) belong to Ga contamination from FIB milling. Observed Cu peaks (k-α: 8.05 and 8.03 KeV, k-β: 8.905 KeV) are from TEM grid and could not be avoided.

Elemental mapping were performed to show the location of Hf nano-clusters. As seen in Figure 4.27, these maps suggest the presence of these clusters at the surface and in the vicinity of precipitates. The positive enthalpy of mixing between Mg and Hf (ΔH=+10 kJ.mole^{-1}) [16], as evidenced by virtually zero solubility in Hf-Mg phase diagram, acts as a driving force for Hf to segregate out even at such small concentrations. These Hf clusters have a negative enthalpy of mixing with Sn atoms (ΔH=-35 kJ.mole^{-1}) [16], and can form co-segregates as shown in Figure 4.22. Co-segregated clusters act as additional nucleation centers for Mg_2Sn formation, hence leading to improvement of aging kinetics and precipitate size refinement. The substantial improvement in precipitate state in T5-0.8Hf over T5 can clearly be seen by comparison HAADF images in Figure 4.24.

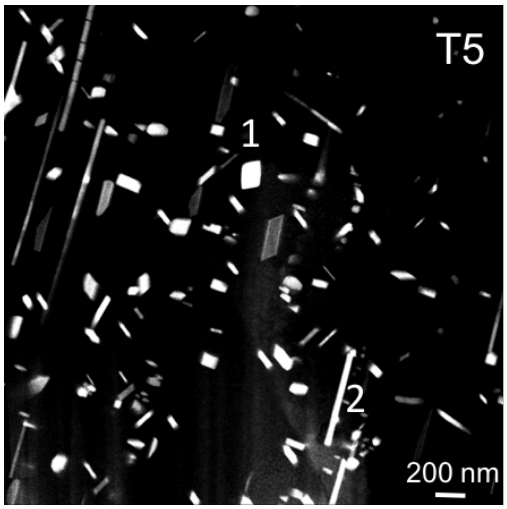

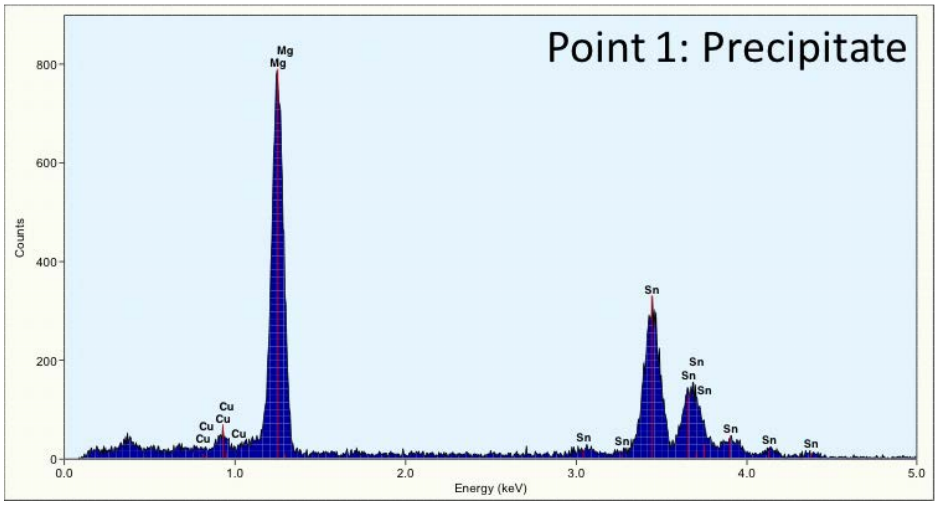

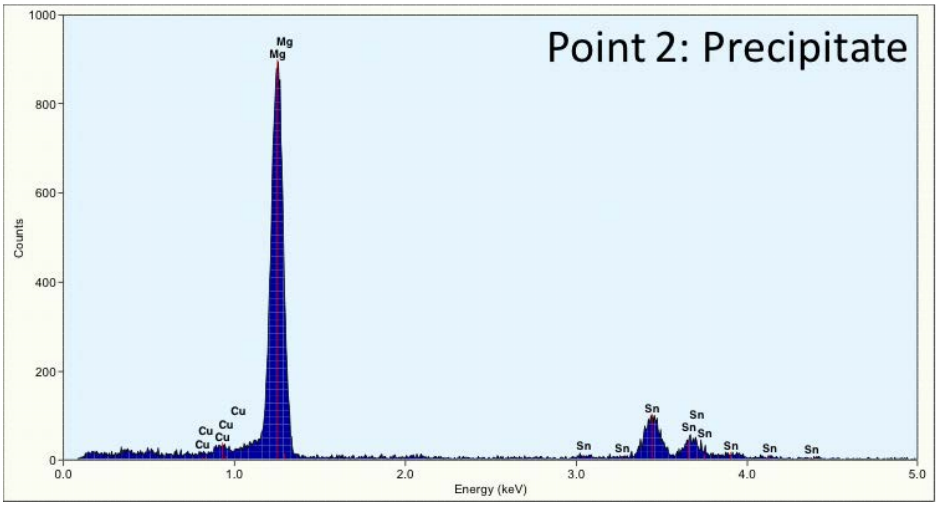

Figure 4.25. EDX analysis of T5 sample

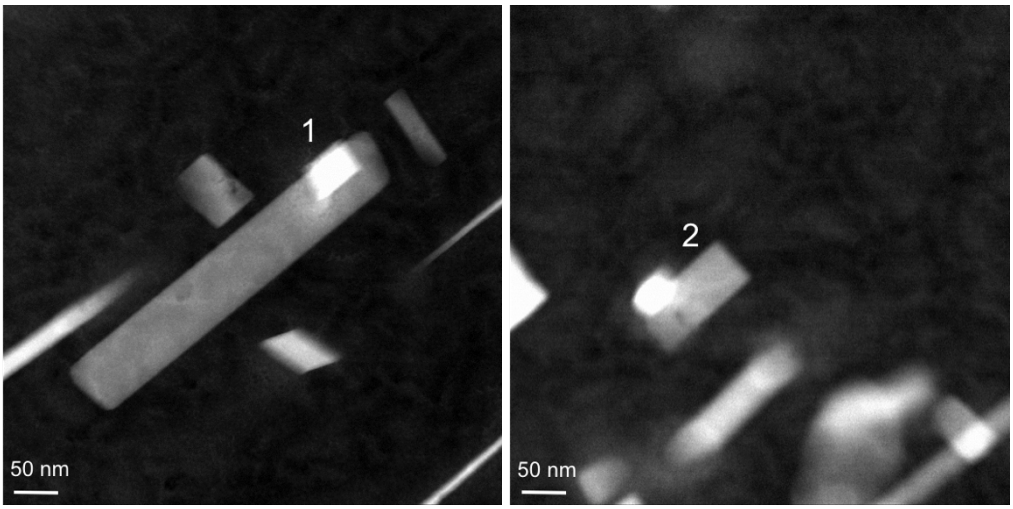

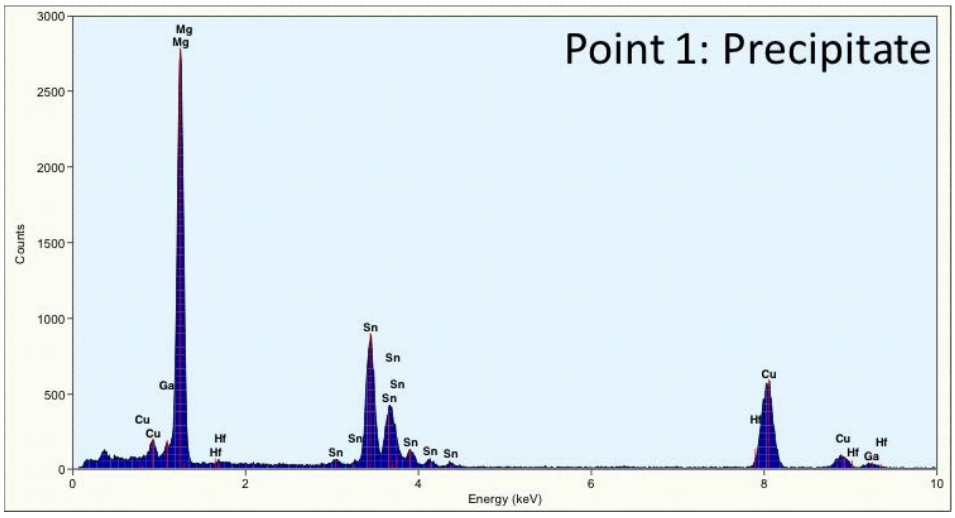

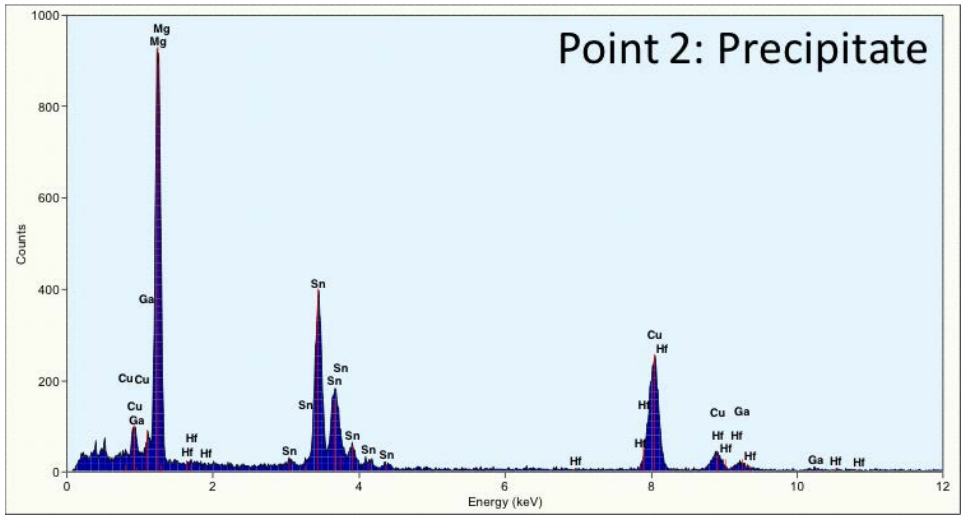

Figure 4.26. EDX analysis of T5-0.8Hf sample

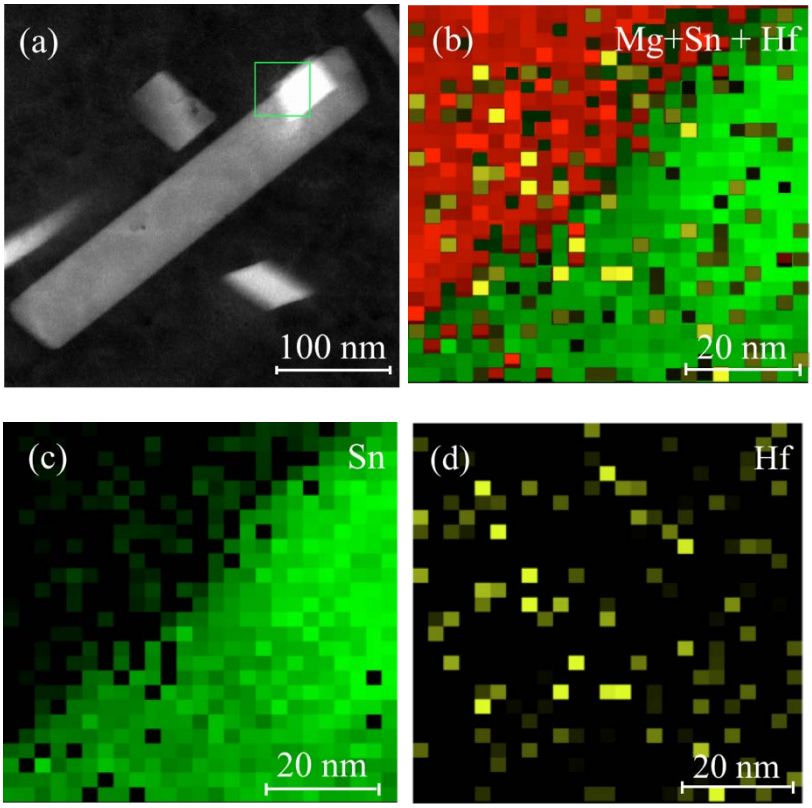

Figure 4.27. Elemental mapping at precipitate-matrix interface
HAADF– Low magnification STEM image of T5-0.8Hf alloy peak aged at 200 °C, and EDX mapping of green box showing (b) Mg (red)+Sn+Hf superimposed map, (c) Sn distribution (green), and (d) Hf distribution (yellow).

Nano-mechanical Testing

For nano-mechanical studies constant load method was applied to analyze and compare nano-indentation creep behavior of the samples. In indentation creep experiments, the representative stress is calculated by dividing the applied load *P* to the projected contact area A_p ,

$$\sigma = {}^{P}/_{A_P} \qquad \text{Equation 4.2.}$$

Projected contact area for an ideal Berkovich indenter is a function of contact depth *h*:

$$A_P = 3\sqrt{3}\,h^2 \tan^2(65.3) = 24.5\,h^2 \qquad \text{Equation 4.3.}$$

For more accurate measurement of the contact area, usually probe area calibration is performed before the test by making several indents on a standard sample of known hardness and modulus such as fused quartz. Then a polynomial function is fitted to these data and projected contact area can be calculated as follows:

$$A_P = 24.5\,h^2 + C_1 h^{1/2} + C_2 h^{1/4} + C_3 h^{1/8} + \cdots \qquad \text{Equation 4.4.}$$

According to Mayo and Nix [17], the strain rate $\dot{\varepsilon}$ for a pyramidal indenter is given as:

$$\dot{\varepsilon} = \frac{1}{h}\frac{dh}{dt} \qquad \text{Equation 4.5.}$$

Secondary creep rate (steady-state) under the power-law regime is related to the stress as [18]:

$$\dot{\varepsilon} = C\,\sigma^{n}\exp\left(\frac{-Q}{RT}\right) \qquad \text{Equation 4.6.}$$

where Q is the activation energy for creep, R is the gas constant, T is the absolute temperature of the test, n is the stress exponent, and C is a constant. By plotting strain rate versus stress in a logarithmic plot, the slope of the fitted line would yield the value of stress exponent *n.* Previous studies show that this value of stress exponent can be compared to that of uniaxial tension creep to determine the mechanism of creep [19-21]. Table 4.7 presents different mechanism responsible, their constitutive equations, and corresponding stress exponents for power-law creep in Magnesium; where b is the magnitude of the Burgers vector, G is shear modulus, and d is grain size. A and m are materials constants. D is either the grain boundary diffusion coefficient (D_{gb}), or lattice diffusion coefficient (D_1), or dislocation pipe diffusion coefficient (D_p).

Table 4.7. Different mechanisms of power-law creep in Magnesium

Mechanism	Constitutive Equation	Stress Exponent (*n*)
Nabarro-Herring diffusional flow	$\dot{\varepsilon} = A_1 \left(\frac{Gb^3}{kT}\right) \frac{D_1}{d^2} \left(\frac{\sigma}{G}\right)$	1
Coble diffusional flow	$\dot{\varepsilon} = A_2 \left(\frac{Gb^3}{kT}\right) \frac{b\, D_{gb}}{d^3} \left(\frac{\sigma}{G}\right)$	1
Harper-Dorn Slip	$\dot{\varepsilon} = A_3 \left(\frac{Gb^2}{kT}\right) \frac{D_1}{b^2} \left(\frac{\sigma}{G}\right)$	1
Lattice diffusion controlled grain boundary sliding	$\dot{\varepsilon} = A_4 \frac{D_1}{d^2} \left(\frac{\sigma}{G}\right)^2$	2
Grain boundary diffusion controlled g.b. sliding	$\dot{\varepsilon} = A_5 \frac{b\, D_{gb}}{d^3} \left(\frac{\sigma}{G}\right)^2$	2
Pipe diffusion controlled grain boundary sliding	$\dot{\varepsilon} = A_6 \frac{D_p}{d^2} \left(\frac{\sigma}{G}\right)^4$	4
Lattice diffusion controlled slip	$\dot{\varepsilon} = A_7 \frac{D_1}{b^2} \left(\frac{\sigma}{G}\right)^5$	5
Pipe diffusion controlled slip	$\dot{\varepsilon} = A_8 \frac{D_p}{b^2} \left(\frac{\sigma}{G}\right)^7$	7

In order to choose the optimum dwell time to calculate stress exponents, at first the highest and lowest limits for holding time were determined by considering thermal drift and steady-state creep assumption. In nano-indentation creep, running experiments with long holding times requires proper control of thermal drift. Therefore, loading cycles with different dwell times (≤2500 seconds, which is the instrument's buffer limit) were examined to find out the higher cap of the dwell time. For holding times longer than 400 seconds, drift related irregularities were observed in the load-displacement graphs.

On the other hand, all the above-mentioned indentation creep equations assume steady-state creep. This assumption sets the lower limit for the holding time. Different holding times of 1, 2, 3, 4, 5, 6 minutes were tested. Strain rate was plotted against time to determine the minimum time required to observe a steady-state strain rate. As can be seen in Figure 4.28, steady-state strain rate was not obtained for holding times less than 5 minutes. Hence a holding time of 6 minutes was chosen for extraction of stress exponents.

It should be noted that since the nano-indenters are often fine tuned for high-resolution displacement measurements, the data acquisition rate of these instruments is relatively high. In order to remove the noise from the data, an exponential function was fitted to displacement data as shown in Equation 4.7, where *a*, *b*, and *C* are fitting parameters. Figure 4.29 shows a typical displacement versus time during the holding section of the loading cycle along with the fitting constants. As can be seen Equation 4.7 was found to fit the creep curves very well.

$$h(t) = a\,t^{b} + C \qquad \text{Equation 4.7.}$$

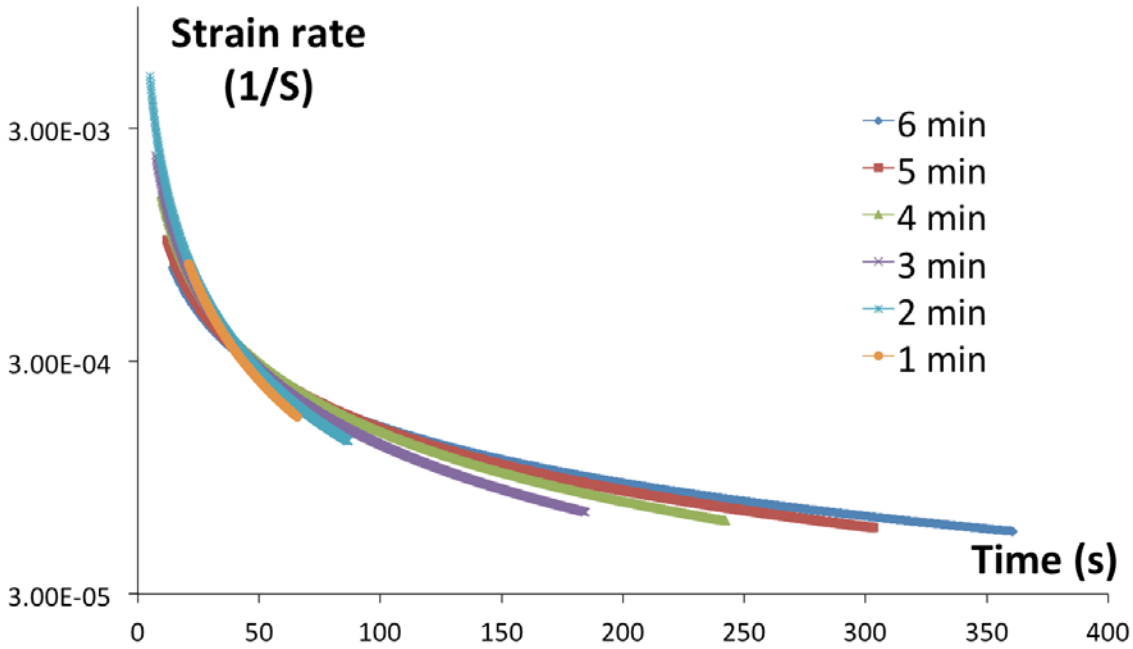

Figure 4.28. Strain rate versus time for different dwell times

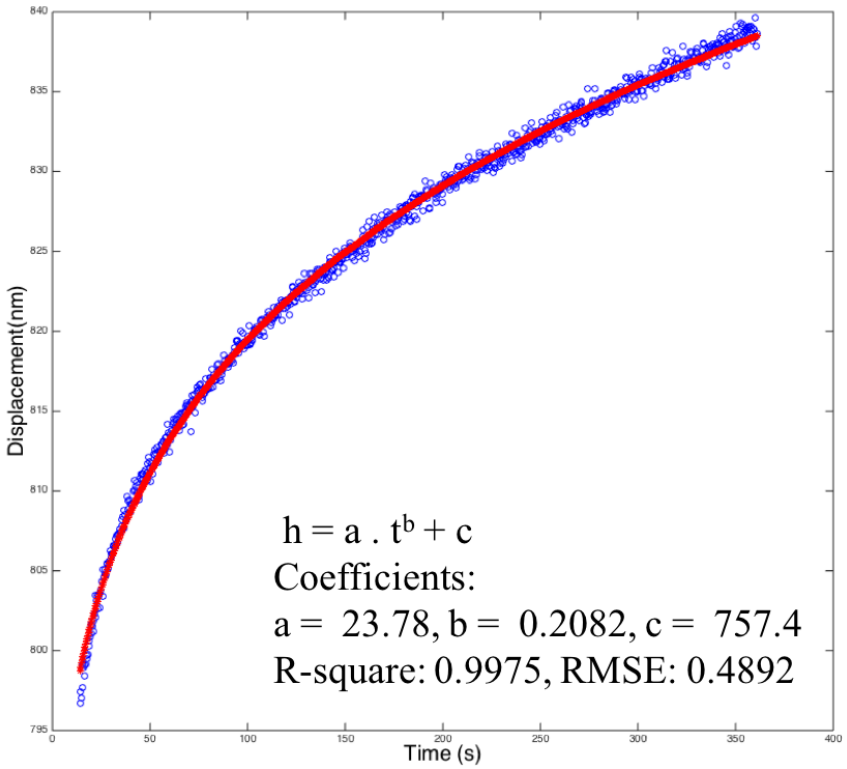

Figure 4.29. Displacement-Time data from nano-indentation and fitting constants

For extraction of stress exponent, first normalized stress was calculated by using the following equation for estimation of shear stress *G* at room temperature for pure Magnesium [22]*:*

$$G(MPa) = 19{,}200\ - 8.6\,T\ (k) \qquad \text{Equation 4.7.}$$

which gives a shear stress of 16,637 MPa for shear stress at 298 *k*. As can be seen in Figure 4.30, normalized stress (σ/G) is around 0.036 in the beginning and then falls to 0.029 at the end of the holding segment. If the normalized stress is in higher than 10^{-3} , the data are in the range for power-law breakdown. The stress range in nano-indentation data is about 30 times more than this critical stress. Although R-square values for a power-law fit were all higher than 0.99, stress exponents are higher than those common in the power-law regime. Calculated stress exponents based on a power-law fit are shown in Table 4.8. Since the stress is also in the range of power-law breakdown, strain rate versus stress data was fitted to an exponential function to check the likelihood of power-law break-down.

Table 4.8. Calculated stress exponents based on power-law assumption

Alloy designation	Power-law stress Exponent (n)	R-square
T5	29.81	0.994
T5-0.2Ti	26.20	0.991
T5-0.8Hf	26.45	0.993
T5-0.4Ti	25.74	0.997
T5-1.5Hf	26	0.995

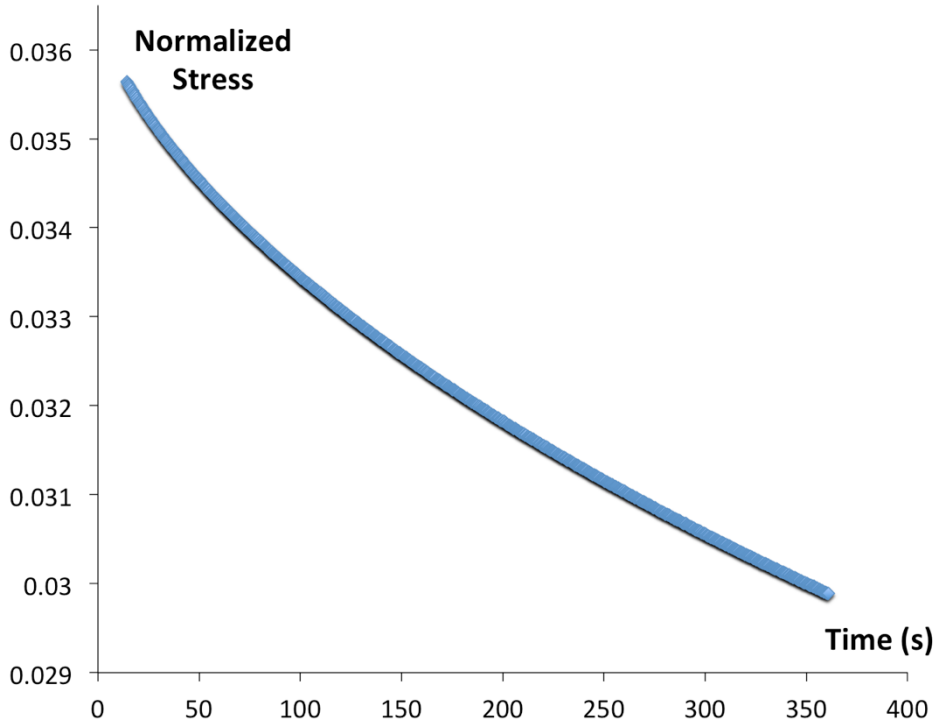

Figure 4.29. Normalized Stress-Time data from nano-indentation

The stress exponent values for power-law break-down are presented Table 4.9. As can be seen the stress exponents decrease in microalloyed compositions, which shows stress dependence of Mg-Sn binary alloy is higher than microalloyed compositions. The average grain size in all the samples is much higher than the size of the indent. So grain boundary controlled creep mechanisms are not responsible in this case.

Power-law breakdown is associated with dislocation glide in hcp metals [23]. Dislocation glide is an easy mechanism in hcp metals unless it is interrupted by obstacles such as precipitates, grain boundaries, solute atoms or other dislocations [23]. Dislocations glide between these obstacles and then climb when reaching them. The higher the applied stress, the faster this climb and the lesser the height to which the dislocations have to

climb before externally applied stress can push them through the internal stress field around the obstacles.

In microalloyed compositions, number density of the precipitates is much higher as evidenced by TEM micrographs in the previous section. Precipitates are also more uniformly distributed in these alloys. This means that the average length of these obstruction-free jogs (dislocation glide) is shorter for modified compositions and climb events become more frequent. When two different creep mechanism work in series, the rate of slower mechanism controls overall creep rate. Therefore, as the precipitates density increases, the stress exponent will be reduced because internal stresses opposing dislocation glide increase and dislocation climb dominates.

Table 4.9. Calculated stress exponents for power-law breakdown

Alloy designation	Power-law breakdown stress Exponent (n')	R-square
T5	5.85 E-08	0.997
T5-0.2Ti	3.89 E-08	0.997
T5-0.8Hf	4.49 E-08	0.998
T5-0.4Ti	3.63 E-08	0.998
T5-1.5Hf	4.06 E-08	0.998

References:

1. Mendis C, Bettles C, Gibson M, Gorsse S, Hutchinson C. Refinement of precipitate distributions in an age-hardenable Mg–Sn alloy through microalloying. *Philosophical magazine letters*. 2006;86(7):443-456.

2. Elsayed F, Sasaki T, Mendis C, Ohkubo T, Hono K. Compositional optimization of Mg–Sn–Al alloys for higher age hardening response. *Materials Science and Engineering: A*. 2013;566:22-29.

3. Mendis C, Bettles C, Gibson M, Hutchinson C. An enhanced age hardening response in Mg–Sn based alloys containing zn. *Materials Science and Engineering: A*. 2006;435:163-171.

4. Buha J. Natural ageing in magnesium alloys and alloying with ti. *J Mater Sci*. 2008;43(4):1220-1227.

5. StJohn D, Cao P, Qian M, Easton M. A brief history of the development of grain refinement technology for cast magnesium alloys. *Magnesium Technology 2013*. 2013:1-8.

6. Lee Y, Dahle A, StJohn D. The role of solute in grain refinement of magnesium. *Metallurgical and Materials Transactions A*. 2000;31(11):2895-2906.

7. StJohn D, Easton M, Qian M, Taylor J. Grain refinement of magnesium alloys: A review of recent research, theoretical developments, and their application. *Metallurgical and Materials Transactions A*. 2013;44(7):2935-2949.

8. Greer A, Bunn A, Tronche A, Evans P, Bristow D. Modelling of inoculation of metallic melts: Application to grain refinement of aluminium by Al–Ti–B. *Acta Materialia*. 2000;48(11):2823-2835.

9. Greer A. Grain refinement of alloys by inoculation of melts. *Philosophical Transactions of the Royal Society of London A: Mathematical, Physical and Engineering Sciences*. 2003;361(1804):479-495.

10. StJohn D, Qian M, Easton M, Cao P. The interdependence theory: The relationship between grain formation and nucleant selection. *Acta Materialia*. 2011;59(12):4907-4921.

11. Nayyeri G, Mahmudi R. The microstructure and impression creep behavior of cast, Mg–5Sn–xCa alloys. *Materials Science and Engineering: A*. 2010;527(7):2087-2098.

12. Sasaki T, Oh-Ishi K, Ohkubo T, Hono K. Enhanced age hardening response by the addition of zn in Mg–Sn alloys. *Scr Mater*. 2006;55(3):251-254.

13. Mendis C, Oh-Ishi K, Hono K. Enhanced age hardening in a Mg–2.4 at.% zn alloy by trace additions of ag and ca. *Scr Mater*. 2007;57(6):485-488.

14. Sasaki T, Oh-Ishi K, Ohkubo T, Hono K. Effect of double aging and microalloying on the age hardening behavior of a Mg–Sn–Zn alloy. *Materials Science and Engineering: A*. 2011;530:1-8.

15. Nie X, Guan Y, Zhao D, et al. Transmission electron microscopy analysis of the crystallography of precipitates in mg-sn alloys aged at high temperatures. *Journal of Applied Crystallography*. 2014;47(5):1729-1735.

16. De Boer FR, Mattens W, Boom R, Miedema A, Niessen A. Cohesion in metals. . 1988.

17. Mayo M, Nix W. A micro-indentation study of superplasticity in pb, sn, and sn-38 wt% pb. *Acta Metallurgica*. 1988;36(8):2183-2192.

18. Goodall R, Clyne T. A critical appraisal of the extraction of creep parameters from nanoindentation data obtained at room temperature. *Acta materialia*. 2006;54(20):5489-5499.

19. Nautiyal P, Jain J, Agarwal A. A comparative study of indentation induced creep in pure magnesium and AZ61 alloy. *Materials Science and Engineering: A*. 2015;630:131-138.

20. Han L, Northwood DO, Nie X, Hu H. The effect of cooling rates on the refinement of microstructure and the nanoscale indentation creep behavior of Mg–Al–Ca alloy. *Materials Science and Engineering: A*. 2009;512(1):58-66.

21. Takagi H, Dao† M, Fujiwara‡ M, Otsuka M. Experimental and computational creep characterization of Al–Mg solid-solution alloy through instrumented indentation. *Philosophical Magazine*. 2003;83(35):3959-3976.

22. Nayyeri G, Mahmudi R. Enhanced creep properties of a cast Mg–5Sn alloy subjected to aging-treatment. *Materials Science and Engineering: A*. 2010;527(18):4613-4618.

23. Gittus J. Creep, viscoelasticity, and creep fracture in solids. . 1975.

5. Conclusion

The objective of this research was to explore the possibility of developing new ternary Magnesium-Tin alloys by microalloying. The criteria for judgment were the effect of microalloying additions on aging kinetics, refinement of precipitate size, and mechanical properties. Our results establish that microalloying with Hafnium and Titanium can tackle some of the issues arising from sluggish precipitate formation kinetics and precipitate size distribution in binary Mg-Sn alloys. Hence, Mg-Sn-Ti and Mg-Sn-Hf alloys can be a potential alternative to replace Rare Earth containing Magnesium alloys.

Since most Rare Earth elements are exported from overseas to US, the price range for AE42 and other existing commercial Mg-RE alloys is very high. There is a need for an alloy that can be made from available natural resources in US, so that the final price and availability of the product is controlled by and not imposed on the US market. Mg-Sn ternary alloys can address this demand in the market. These new alloys also offer an order of magnitude reduction in heat treatment time (from approximately 1000 hours to less than 100 hours), which makes the benefits of their application two-fold by decreasing manufacturing energy costs and production time. This can also open the route for development of an age-hardenable wrought Mg alloy.

Mg-Sn-Ti and Mg-Sn-Hf alloys can bring significant change to the current state of the art. Under president's initiative, new EPA and the National Highway Traffic Safety Administration (NHTSA) regulations force automotive companies to reduce their emissions by 2017. Altogether, cars and light trucks use about 45% of oil consumed in US. The potential weight reduction in the US automotive market alone leads to 100 billion gallons of gas and 6.5 billion gallons of CO_2 emissions per year.

In defense and aerospace market, China is the leading foreign supplier of rare earths necessary for fabrication of current Mg alloy counterparts, making core defense technologies vulnerable to interruption of Chinese imports. In the past, China has used its control over mining, application and import of rare earths as a strategic leverage [1]. These new alloys offer an alternative that can be made from domestic resources improving national security and minimizing foreign dependence.

However, some of the aspects of alloy development and application require further investigation and investment before commercial production. A list of suggestions for future research on these alloys is summarized in the next section.

6. Recommendations for Future Work

Suggestions for future work can be categorized as follows:

Alloy Development Method

In present study, alloys were synthesized under controlled atmosphere in the glovebox, but industrial production of Mg alloys is usually done by using a flux or flux-less melting in air with aid of CO_2 or SF_6 [2]. Microalloying needs precise control of minute additions of the ternary alloying element; recovery rates of alloying elements are affected by alloying method. Therefore, the effect of alloying method on composition has to be well studied before large scale production.

Composition Optimization

A more thorough study on the alloy formulation is required to determine the optimum amount of Hafnium and Titanium additions. Author recommends indirect addition of Hf or Ti in the form of Sn-Hf or Sn-Ti master alloys as it allows more precise addition of the alloying elements and insures better mixing. It would be ideal if the compositions are measured by characterization methods such as ICP-MS in order that exact amounts of microalloying element present in the bulk of the final product can be measured.

Diffusion Experiments

Precipitate growth kinetics in Mg-Sn system is affected by interdiffusion of Sn and Mg. Current theories are solely based on phenomenological analysis. Study of the effect of microalloying element on the diffusivity of Tin and Magnesium can shed light on the mechanisms through which microalloying elements improve ageing kinetics.

At-temperature Mechanical Testing

At temperature tests at elevated temperatures to compare creep behavior of these alloys with that of Mg-RE alloys is required to validate the advantage of the proposed Mg-Sn ternary alloys.

Computational Thermodynamics

Development of ternary phase diagrams of Mg-Sn-Na, Mg-Sn-Ti, and Mg-Sn-Hf can provide a unique tool for composition optimization. Also, it is a huge step to better clarify the possible mechanisms for the observed differences between Na, Ti and Hf. Consequently, such clarification can be used for selection of microalloying elements for other binary alloys of Magnesium.

Grain Refinement

A more elaborate investigation of grain refinement in Mg-Sn system by Ti addition is beneficial in finding out if the particle size is in fact the determining factor for the observed grain refinement. Precise monitoring of heat transfer during casting would be essential in such experiments.

Corrosion Performance

Addition of certain metals such as Iron even at trace levels can have drastic effects on the corrosion performance of Mg alloys. It is necessary to study the effect of Hf and Ti additions on corrosion behavior of the alloy. Such research is critical to extending application of microalloyed compositions to new markets such as biomedical and orthopedics

References:

1. Grasso VB. Rare earth elements in national defense: Background, oversight issues, and options for congress. . 2013.

2. Friedrich HE, Mordike BL. *Magnesium technology.* Springer; 2006.

VITAE

SADEGH BEHDAD

EDUCATION

2001-2006	Polymer Engineering, BSc Amirkabir University of Technology, Tehran, Iran
2007	1st in the nationwide MSc entrance exam in Iran
2007-2009	Polymer Engineering, MSc Amirkabir University of Technology Tehran, Iran
2010-2015	Materials Science and Eng., PhD Florida International University Miami, Florida
2012	NSF Student Travel Grant Award to attend ASME IMECE
2014	DEA Fellowship University Graduate School Florida International University
2015	DYF Fellowship University Graduate School Florida International University

PUBLICATIONS

1. Direct observation of carbon nanotube (CNT) induced strengthening in aluminum composite via in situ tensile tests Carbon, 69, 2014, P. 79–85, B. Boesl, D. Lahiri, S. Behdad and A. Agarwal

2. Diffusion Kinetics, Mechanical Properties, and Crystallographic Characterization of Intermetallic Compounds in the Mg-Zn Binary System Intermetallics, 67, 2015, P. 145-155, C.C. Kammerer, S. Behdad, L. Zhou, F. Betancor, M. Gonzalez, B. Boesl, Y.H. Sohn

3. Improvement of Aging Kinetics and Precipitate Size Refinement in Mg-Sn alloys by Hafnium Additions Materials Sci. and Eng. A, 2015, In Press (http://dx.doi.org/10.1016/j.msea.2015.11.043), S. Behdad, L. Zhou, H. Henderson, M. Manuel, Y. Sohn, A. Agarwal, and B. Boesl

4. Structural and mechanical properties changes induced in nanocrystalline ZrC thin films by Ar ion irradiation Journal of Nuclear Materials, 2015, In Press (http://dx.doi.org/10.1016/j.jnucmat.2015.11.012), D. Craciun, G. Socol, D. Simeone, S. Behdad, B. Boesl, B.S. Vasile, V. Craciun

5. Ar ions irradiation effects in ZrN thin films grown by pulsed laser deposition Applied Surface Science, 336, 2015, P. 129–132, D. Craciun, G. Socol, G. Dorcioman, D. Simeone, D. Gosset, S. Behdad, B. Boesl

6. Effect of addition of hydrophobic nano silica on viscoelastic properties and scratch resistance of an acrylic/melamine automotive clearcoat Tribology International, 43, 2010, P. 685–693, N. Tahmassebi, S. Moradian, B. Ramezanzadeh, A. Khosravi, S. Behdad